

# Triggers of the 2022 Larsen B multi-year landfast sea ice break-out and initial glacier response

Naomi E. Ochwat<sup>1,2\*</sup>, Ted A. Scambos<sup>1</sup>, Alison F. Banwell<sup>1</sup>, Robert S. Anderson<sup>2</sup>, Michelle L. Maclennan<sup>3</sup>, Ghislain Picard<sup>4</sup>, Julia A. Shates<sup>5</sup>, Sebastian Marinsek<sup>6</sup>, Liliana Margonari<sup>6</sup>, Martin Truffer<sup>7,8</sup>, and Erin C. Pettit<sup>9</sup>

<sup>1</sup>Earth Science Observation Center (ESOC), Cooperative Institute for Research in Environmental Sciences (CIRES), University of Colorado Boulder, Boulder, CO, USA

<sup>2</sup>Department of Geology, University of Colorado Boulder, Boulder, CO, USA,

<sup>3</sup>Department of Atmospheric and Oceanic Sciences, University of Colorado Boulder, Boulder, CO, USA,

<sup>4</sup>Univ. Grenoble Alpes, CNRS, Institut des Géosciences de l'Environnement (IGE), UMR 5001, Grenoble, France

<sup>5</sup>Department of Atmospheric and Oceanic Sciences, University of Wisconsin–Madison, Madison, WI, USA

<sup>6</sup>Instituto Antártico Argentino, Buenos Aires, Argentina

<sup>7</sup>Geophysical Institute, University of Alaska Fairbanks, Fairbanks, AK, USA,

<sup>8</sup>Department of Physics, University of Alaska Fairbanks, Fairbanks, AK, USA

<sup>9</sup>College of Earth, Ocean, and Atmospheric Sciences, Oregon State University, Corvallis, OR, USA

\*correspondence to: N. Ochwat ([naomi.ochwat@colorado.edu](mailto:naomi.ochwat@colorado.edu))

## Abstract

In late March 2011, landfast sea ice (hereafter, ‘fast ice’) formed in the northern Larsen B embayment and persisted continuously as multi-year fast ice until January 2022. In the 11 years of fast ice presence, the northern Larsen B glaciers slowed significantly, thickened in their lower reaches, and developed extensive mélange areas leading to the formation of ice tongues that extended up to 16 km from the 2011 ice fronts. In situ measurements of ice speed on adjacent ice shelf areas spanning 2011 to 2017 show that the fast ice provided significant resistive stress to ice flow. Fast ice breakout began in late January 2022, and was closely followed by retreat and break-up of both the fast ice mélange and the glacier ice tongues. We investigate the probable triggers for the loss of fast ice and document the initial upstream glacier responses. The fast ice break-up is linked to the arrival of a strong ocean swell event (>1.5 m amplitude; wave period waves >5 s) originating from the northeast. Wave propagation to the ice front was facilitated by a 12-year low in sea ice concentration in the northwestern

30 Weddell Sea, creating a near-ice-free corridor to the open ocean. Remote sensing data in the months following the fast ice  
31 break-out reveals an initial ice flow speed increase ( $> 2$ -fold), elevation loss (9 to 11 m), and rapid calving of floating and  
32 grounded ice for the three main embayment glaciers Crane (11 km), Hektoría (25 km), and Green (18 km).

## 33 **1 Introduction**

34 As the climate warms, ice shelves in Antarctica are predicted to become more susceptible to collapse (Mercer, 1978; Gilbert  
35 and Kittel, 2021). In the late 1980s and mid 1990s several ice shelves along the Antarctic Peninsula (AP) coast retreated and  
36 eventually disintegrated, including the Wordie, Prince Gustav, Larsen Inlet, Larsen A ice shelves, and in March 2002, the  
37 northern two-thirds of the Larsen B Ice Shelf (Rott et al., 1996; Glasser and Scambos, 2008; Cook and Vaughan, 2010). In  
38 2008 and 2009, several smaller break-up events occurred on the Wilkins Ice Shelf (Braun et al., 2009; Scambos et al., 2009).  
39 There has been significant research elucidating the causes of these collapses, focusing on both ice-shelf thinning due to basal  
40 and surface melting (Smith et al., 2020), as well as lake drainage mechanisms related to surface meltwater-induced ice-shelf  
41 flexure and hydrofracture (Doake and Vaughan 1991; Scambos et al., 2000; Scambos et al., 2003; Banwell et al., 2013; Banwell  
42 and MacAyeal, 2015) partly attributed to warmer climate conditions (Rott et al., 1998), plate-bending stresses on the ice-shelf  
43 front (Scambos et al., 2009), and ocean swell flexure (Massom et al., 2018). Massom et al. (2018) further implicate loss of fast  
44 ice and ocean swell in the Wilkins Ice Shelf breakup events, following loss of a protective pack ice buffer offshore – due to  
45 the vulnerability of fast ice to ocean swells (Crocker and Wadhams, 1989; Langhorne et al., 2001). While fast ice is  
46 consolidated sea ice that remains stationary attached to the coast and can be annual or perennial (Fraser et al., 2021), pack ice  
47 refers to sea ice that is comprised of separate floes and is under the influence of winds and ocean currents. The loose structure  
48 of pack ice has a strong damping effect on ocean swell (Squire, 2007).

49 Intense surface melt events on the eastern Antarctic Peninsula have been linked to atmospheric rivers (ARs; Wille et al., 2019;  
50 Wille et al., 2022) and foehn winds (Cape et al., 2015; Datta et al., 2019; Laffin et al., 2022). ARs are long narrow bands of  
51 warm and moist air that can cause extreme warm temperatures, increase surface melting, advect sea ice away from the ice  
52 edge, reduce sea ice concentrations, and generate foehn events (Bozkurt et al., 2018; Wille et al., 2022; Liang et al., 2023).  
53 Foehn events occur when a moist air mass ascends on the windward side of a mountain range or ridge and cools at the (lower)  
54 wet-adiabatic rate, while losing moisture to precipitation. It then descends over the lee side, adiabatically warming at the higher  
55 dry-air rate, resulting in an increase in temperature. The loss of ice shelves can substantially reduce the stability of tributary  
56 outlet glaciers, leading to acceleration, increased calving, thinning, and ultimately, sea level rise. For example, when the Larsen  
57 B collapsed in 2002, Crane Glacier thinned by  $25 \text{ m yr}^{-1}$  over much of its length (Needell and Holschuh, 2023) and immediately  
58 sped up by roughly 3-fold (Rignot et al., 2004) and the Hektoría-Green-Evans (hereafter, HGE) Glacier system ice flow speed  
59 increased by up to 8-fold (Rignot et al., 2004). After the collapse of the Larsen B in 2002, the embayment was frequently filled  
60 by seasonal sea ice (landfast and pack ice). However, in late March 2011, landfast sea ice (hereafter ‘fast ice’) formed in the

61 Larsen B embayment, and the interior two-thirds of the embayment was continuously covered by multi-year fast ice until  
62 January 2022. On 19 January 2022, this fast ice cover was suddenly fractured and began to drift out, leading within days to  
63 retreat and break-up of the tributary glacier mélange and floating ice tongue areas (Fig. 1). Fast ice has been shown to stabilize  
64 outlet glaciers by reducing calving (Amundson et al, 2010; Robel 2017) and suppressing wave action against the outlet glacier  
65 (Murty, 1985; Langhorne et al., 2001) causing the glacier terminus to advance (Reeh et al., 2001). When fast ice or mélange  
66 breaks up, ice-shelf calving resumes, sometimes releasing several decades of accumulated ice flux, and exposing the new  
67 terminus to ocean dynamics (Reeh et al., 2001; Cassotto et al., 2015).

68 Several studies have suggested that break-up of fast ice can reduce the structural integrity of ice shelves and ultimately lead to  
69 their collapse (Khazendar et al., 2007; Massom et al., 2010; Borstad et al., 2013; Banwell et al., 2017; Massom et al., 2018).  
70 There have been many examples of tributary glacier acceleration and significant ice front retreats following the removal of  
71 fast ice or pack ice in Greenland and Antarctica (Miles et al., 2017, Miles et al., 2018, Gomez-Fell et al., 2022). Others (Sun  
72 et al., 2023; Surawy-Stepney et al., 2023) suggest that fast ice does not provide sufficient buttressing (resistive stress to impact  
73 the system dynamics.

74 Here we investigate the climatic and oceanic drivers that led to the rapid break-out of the decade-old Larsen B fast ice in  
75 January 2022, while also drawing parallels to previous fast ice and ice shelf collapses. We then assess the initial glacier  
76 dynamic response to the loss of the buttressing fast ice by evaluating changes in velocity, terminus position, and elevation of  
77 the Crane, Jorum, Punchbowl, and HGE glaciers. A preliminary assessment of the cause of the fast ice break-up was discussed  
78 as a sidebar in the NOAA State of the Climate 2022 report (Ochwat et al., 2023b). However, the current study evaluates the  
79 events in much greater detail and includes a quantitative look at the glacier response.

80

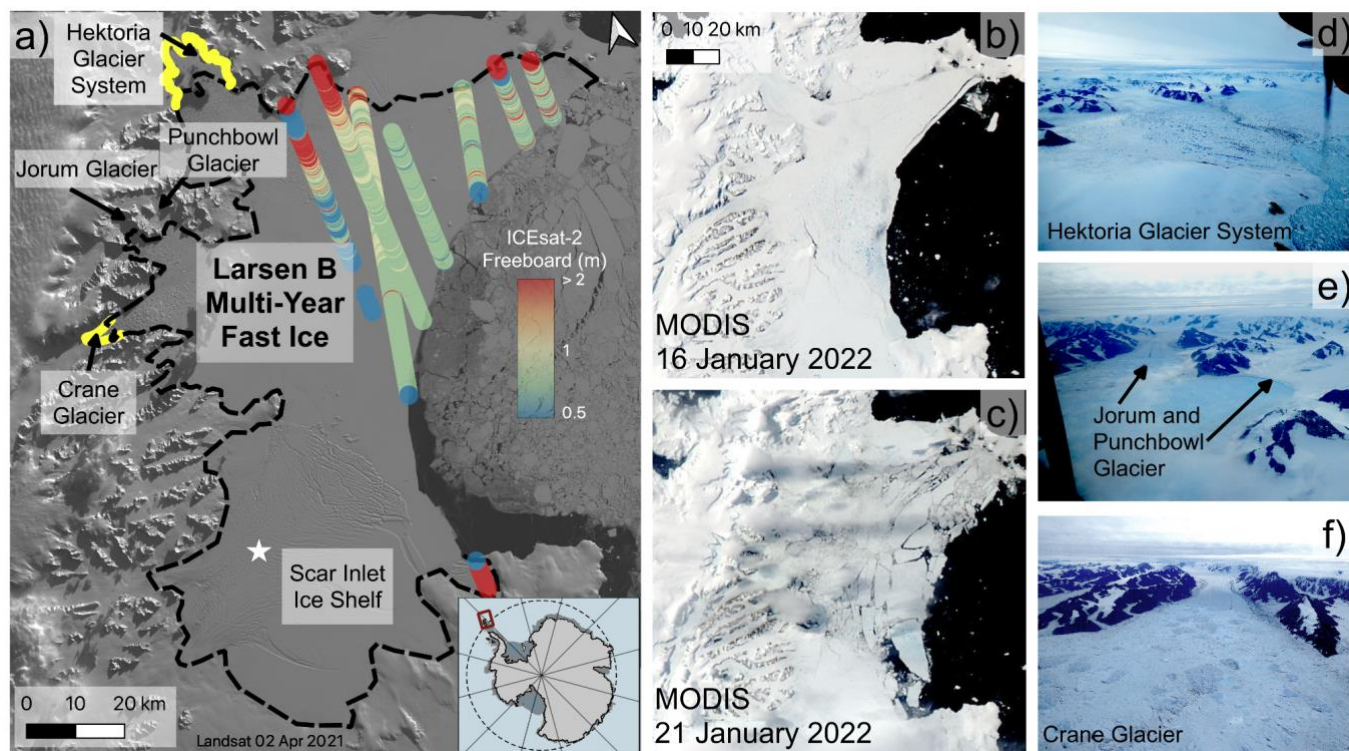
## 81 **2 Study area**

82 The Larsen B embayment (65.24° S, and 61.00° W; Fig. 1) is located on the eastern side of the AP, between Graham Land and  
83 the northwestern Weddell Sea and is ~7000 km<sup>2</sup> in area. North of the embayment is the Seal Nunataks Ice Shelf (Shuman et  
84 al., 2016) and to the south is a remnant of the Larsen B Ice Shelf; the Scar Inlet Ice Shelf. Prior to 1995, the eastern coast of  
85 Graham Land was almost entirely flanked by ice shelves (e.g., Skvarca et al., 1999; Cook and Vaughan, 2010), but after a  
86 series of disintegrations, only the Scar Inlet and Larsen C Ice Shelf remain.

87

88 Due to the elevated narrow ridge of the northern AP (Graham Land) and the prevailing westerly wind, the climate of the Larsen  
89 B embayment region differs greatly between the western and eastern flanks. The ridge obstructs the Southern Hemisphere  
90 westerlies and induces strong orographic lifting and precipitation on the western side, while the eastern side is much drier and  
91 cooler (King et al., 2003; Van Wessem et al., 2015). The climate is heavily influenced by the phase of the Southern Annual  
92 Mode (SAM; Leeson et al., 2017; Fogt and Marshall, 2020). When the SAM index is positive, warming events occur more

93 frequently on the eastern side of the Peninsula due to an increase in westerly flow across the Peninsula (Orr et al., 2008; Van  
94 Lipzig et al., 2008).  
95



96  
97 *Figure 1: a) Freeboard thickness from ICESat-2 data from 1 January 2021 to 1 January 2022. The yellow dashes show the*  
98 *TanDEM-X determined 2016 grounding zone (Rott et al., 2018) and black dashes are a slope change and calving-morphology*  
99 *inferred 2021 grounding zone (this study). An AMIGOS GPS installation on Scar Inlet Ice Shelf is indicated by the white star.*  
100 *The background image is from Landsat 8 2 April 2021. b) MODIS image from 16 January 2022. c) MODIS image from 21*  
101 *January 2022, two days after initial rifts in the fast ice formed. d, e, f) Images captured by a British Antarctic Survey overflight*  
102 *on 31 January, 11 days after the fast ice break-out event.*

### 103 **3 Data and Methods**

104 The following datasets are used in various capacities to evaluate the triggers of the fast ice break-out as well as the initial  
105 glacier response. Reanalysis data is used to evaluate both potential atmospheric and oceanic triggers. Passive microwave data  
106 is used to determine sea ice extent and surface melt conditions. Optical satellite imagery from a number of satellite systems,  
107 and synthetic aperture radar data, are used for assessing glacier ice, fast ice, elevation changes, and determining glacier speeds.  
108 Laser altimetry data is also used for assessing initial glacier and fast ice elevation. Lastly, GNSS data is used to look at Scar  
109 Inlet Ice Shelf speeds.

### 110 **3.1 Reanalysis Data**

111 We used ERA-5 Reanalysis data (Hersbach et al., 2020) at both monthly and hourly temporal resolution to assess temperature  
112 and precipitation anomalies in 2017 to 2022, as well as foehn wind occurrence in the months prior to and including January  
113 2022. To investigate the presence of foehn winds, we followed Laffin et al. (2022), who determined that foehn winds that  
114 produce surface melt require a temperature  $> 0^{\circ}\text{C}$ , a wind speed of  $> 2.85 \text{ m s}^{-1}$ , humidity  $< 79\%$ , and a wind direction from  
115 the north or northwest. These thresholds agree with Cape et al. (2015)’s determination of the onset of “foehn days” (foehn  
116 conditions for greater than 6 hours).

117  
118 To identify ARs during the last two weeks of January 2022, we use hourly ERA-5 to examine vertically integrated water vapor  
119 transport (IVT) bands that extend from the extra-tropics towards the Antarctic ice sheet (Bozkurt et al., 2018; Wille et al.,  
120 2019). IVT is calculated as the vector magnitude of eastward integrated water vapor transport (uIVT) and northward integrated  
121 water vapor transport (vIVT). We identify an AR event during the breakout as a continuous, extended region of locally high  
122 IVT that reaches a peak intensity of almost  $300 \text{ kg m}^{-1} \text{ s}^{-1}$ , consistent with Wille et al. (2022).

123  
124 Following Massom et al. (2018) and Teder et al. (2022), we investigate the occurrence of open-ocean corridors across the sea  
125 ice zone, using ERA-5 and WaveWatch III wave data. We used significant wave height as a proxy for wave energy (Teder et  
126 al., 2022), calculated to be four times the square root of the zeroth moment of the energy density spectrum (Massom et al.,  
127 2018). We used peak wave period as an indication of longer swell wavelengths, which can transmit more energy into the fast  
128 ice plate (Robinson and Haskell, 1992; Massom et al., 2018). Mean wave direction is used to assess alignment with the corridor  
129 axis and propagation toward the ice front. We examined the hourly time series of ocean wave variables for January 2022 at  
130 two different locations, within the corridor and near the Larsen B fast ice front.

### 131 **3.2 Satellite Data**

#### 132 **3.2.1 Passive Microwave Data**

133 We combined passive microwave data from two successive sensors, namely the Advanced Microwave Scanning Radiometer  
134 for the Earth Observing System (AMSR-E) on the Aqua Satellite, and the Advanced Microwave Scanning Radiometer 2  
135 (AMSR-2) on the ‘Shizuku’ (GCOM-W1) satellite. Together, these passive microwave sensors provide nearly continuous  
136 daily data from 2002 until present (apart from a gap from October 2011 to June 2012 between the two satellites’ operation).  
137 The daily overall sea ice concentration data product (Spreen et al., 2008) was used to assess overall sea ice extent and  
138 concentration on the same day (January 19th) for the 12-year period.

139  
140 We also used AMSR-E/2 data to investigate fast ice melt extent for each melt season (October 1 to March 31) from 2011 to  
141 2022. To do this, we followed the algorithm from Torinesi et al. (2003) and methods of Picard et al. (2007). For each 12.5 km

142 grid cell and each day, the liquid water is detected as present if the 19 GHz horizontally-polarized brightness temperature is  
143 higher than a threshold that is empirically determined in each cell and for each year by using the brightness temperatures during  
144 the winter (dry snow) season. ‘Melt days’ are defined as days when meltwater is present on or near the ice surface, but active  
145 melting is not necessarily taking place. Finally, we calculated the total number of melt days for each melt season. We used the  
146 same fully automatic algorithm as used recently in Banwell et al. (2021, 2023) for Antarctic ice shelves. However, for the  
147 current study, a careful visual evaluation of the passive microwave data (brightness temperature timeseries) was done for all  
148 the pixels in proximity to the open ocean. This was necessary because the real footprint of the measurements acquired by the  
149 radiometer is larger than the pixel size and of elliptical shape (14 x 22 km) (Meier et al., 2018). The ellipse’s position and  
150 orientation changes from track to track with respect to the pixels. As a consequence, the fast ice pixel near the shore may be  
151 contaminated by signal coming from the nearby open ocean, hence potentially perturbing the detection of the melt. Our manual  
152 selection prevents this effect.

### 153 **3.2.2 Optical Imagery and Synthetic Aperture Radar**

154 We used MODIS (Moderate-Resolution Spectroradiometer), Landsat 8 and 9, Worldview (WV) -1, 2, and 3, and Synthetic  
155 Aperture Radar (SAR; Sentinel 1) to investigate changes in glacier characteristics and dynamics. The MODIS sensor, on the  
156 Aqua and Terra satellites, has a data archive from 2002 to present and was used to determine the dates of fast ice formation,  
157 seasonal area changes, break-up timing and extent of retreat. The Landsat 8 and 9 Operational Land Imager product was used  
158 to assess melt patterns during the 2021/2022 austral season and to determine ice flow speeds using a Python-based image  
159 cross-correlation software, PyCorr (Fahnestock et al., 2016). PyCorr measures ice displacement between two images by finding  
160 the peaks in normalized cross-correlation surfaces between image chips extracted in a grid pattern over both images. For  
161 images separated by one year, using Landsat 8 and 9 panchromatic images (15 m spatial resolution) error is  $\sim\pm 7.5$  m yr<sup>-1</sup>,  
162 however shorter time intervals result in higher errors (Fahnestock et al., 2016). WV-1, 2, and 3 satellite images have very high  
163 resolution (< 0.5 m) and were used for investigating the morphology of icebergs and the creation of digital elevation models  
164 (DEMs). Worldview in-track stereo-image DEMs (Table S1) were obtained from the Polar Geospatial Center (PGC). The  
165 DEMs have a spatial resolution of 2 m and absolute accuracy of  $\sim 4$  m in horizontal and vertical dimensions (from PGC  
166 documentation). We corrected for the geoid using EGM 2008 and then assessed the mean elevation difference (i.e., bias) for  
167 six bedrock regions in each of the WV DEMs relative to the REMA DEM (Howat et al., 2022) and applied the mean offset to  
168 the WV DEMs, similar to the method used with the ArcticDEM for the Hunt Fjord Ice Shelf in Greenland (Ochwat et al.,  
169 2023a).

170  
171 We assessed calving styles and approximate grounding zone positions using the imagery and DEM data. In Figure 1a, the  
172 yellow dashes show Rott et al.’s (2018) 2016 grounding line, determined by surface elevation changes from TanDEM-X  
173 differencing. The black dashes show a slope change and calving-morphology inferred 2021 grounding line (this study). Our  
174 grounding zone is estimated from a break in slope in the DEMs and morphological changes, such as the appearance of broad

175 surface undulations suggestive of bottom crevassing and changes in calving style at the glacier front. We do not suggest the  
176 grounding line advanced between the two estimates, but arise from the two different determination methods. Our grounding  
177 zone position is similar to the partial grounding zone proposed by Sun et al. (2023) and Tuckett et al. (2020); where a presence  
178 of an ice plain can explain why there are multiple determinations of a grounding zone (Friedl et al., 2019). Calving styles of  
179 grounded ice often show surface slumping or tilting prior to separation, indicative of listric faulting (Parizek et al., 2019),  
180 super-buoyancy (Murray et al., 2015) or ice-cliff stresses (Bassis et al., 2021; Crawford et al., 2021). Further analysis of the  
181 evolution of the grounding zone position and the evolution of calving styles for the lower HGE Glaciers will be assessed in a  
182 later study.

183

184 We used Sentinel-1A and -1B SAR data to estimate ice flow speeds. The Alaska Satellite Facility HyP3 Pipeline uses speckle  
185 tracking to create velocity rasters using SAR image pairs. The HyP3 pipeline utilizes GAMMA and auto-RIFT algorithms  
186 through the Vertex On-Demand Processing Tool (Gardner et al., 2018; Lei et al., 2021). The autoRIFT code includes an  
187 iterative process for determining the flow velocity, with varying relative errors that have an average of 4% for both X and Y  
188 direction velocity (Lei et al., 2021). Sentinel-1A and -B have a repeat time of 6 days when used in combination, and 12 days  
189 if only 1A or 1B pairs are used. Sentinel-1B malfunctioned in December 2021, leaving only Sentinel-1A data available after  
190 that date.

191

192 We extracted ice speed profiles in a band centered on the Airborne Thematic Mapper (ATM) profiles from Operation IceBridge  
193 for Crane, Jorum, Green, and Hektoría glaciers, generating five profiles that span the central 1 km near the approximate glacier  
194 centerlines. To approximate the mean monthly speed, we averaged the speed profile of two 12-day Sentinel-1 cycles.

### 195 **3.2.3 Laser Altimetry**

196 To study changes in surface ice elevation, we combined the WV image-derived DEMs with ICESat-2 altimetry data. We used  
197 the ICESat-2 ATL06 version 5 product, which provides a linear surface approximation of 40 m overlapping segments along  
198 each ground track (Smith et al., 2021) with a 91-day repeat cycle (clouds permitting). We correct for the geoid prior to  
199 estimating the initial thickness of the fast ice, glacier tongues, and elevation of the glaciers. We used ICESat-2 data for the  
200 period January 2021 to December 2021 (Fig. 1) to determine the initial fast ice and glacier tongue freeboard. To account for  
201 tidal variations, we only used tracks that crossed open water (as assessed in MODIS or Sentinel 1 imagery). For Fig. 1, we  
202 applied offsets to each track according to the reported elevation of the open sea surface at the time of acquisition. Assuming  
203 the proportion of snow relative to ice thickness is low, we calculated fast ice thicknesses from the freeboard using the standard  
204 hydrostatic equilibrium floating ice relationship using a density of  $1028 \text{ kg m}^{-3}$  for sea water and  $900 \text{ kg m}^{-3}$  for ice. For  
205 analyzing glacier elevation changes, we extracted ICESat-2 data from where tracks cross  $< 200 \text{ m}$  of near-centerline tracks  
206 flown by Operation IceBridge using the ATM sensor, and averaged the data. Standard error analysis was performed on the

207 individual WV and ICESat-2 elevations. We use the square-root of the sum of the squares of the error, where the errors are the  
208 standard error of the mean and the instrument error of WV or ICESat-2.

### 209 **3.2.4 GNSS data from AMIGOS station on Scar Inlet**

210 An Automated Meteorology-Ice-Geophysics Observing System (AMIGOS) unit with a dual-channel GPS receiver was placed  
211 on the Scar Inlet Ice Shelf in February of 2010 (Scambos et al., 2013) as part of the Larsen Ice Shelf System, Antarctica project  
212 (LARISSA; Wellner et al., 2019). The system provided hourly position data spanning February 2010 through August 2017,  
213 with several data gaps due to power and system malfunctions, that were periodically repaired during re-visits. Precision of the  
214 hourly position data was approximately  $\pm 20$  cm due to wind on the tower mounting of the GPS antenna. We used daily, weekly,  
215 and monthly averaged data to evaluate ice flow of the Scar Inlet Ice Shelf over the formation and thickening period of the  
216 adjacent fast ice.

### 217 **3.2.5 Aerial photography**

218 To evaluate how the fast ice break-up occurred and the potential calving styles of the outlet glaciers, we also analysed airborne  
219 photography. On 31 January 2022, the British Antarctic Survey flew a Twin Otter over the study area with a digital camera  
220 (Panasonic DMC-TZ80e) and a series of photos of the glacier fronts and ice tongue areas were taken along with approximate  
221 geolocation.

## 222 **4 Results**

### 223 **4.1 Multi-year fast ice in the Larsen B embayment**

#### 224 **4.1.1 Formation and evolution of Larsen B multi-year fast ice**

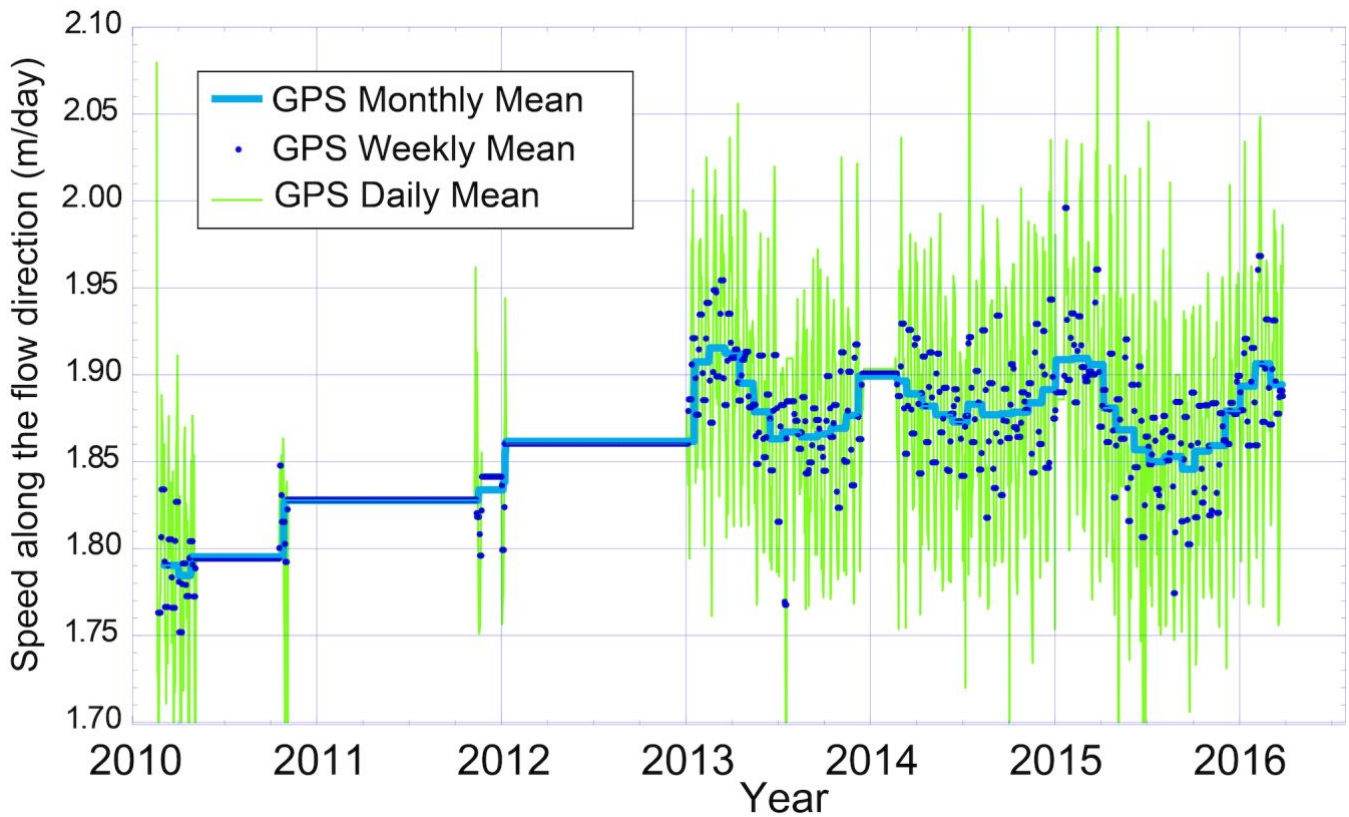
225 The fast ice that formed in March 2011 had a few partial retreats during the 11 years that the interior embayment region was  
226 continuously covered. Portions of the fast ice broke out and reformed in May 2011 and March 2012. From March 2012  
227 onwards, the fast ice maintained a minimum area of  $\sim 3975$  km<sup>2</sup> (based on MODIS imagery). From 2012 to 2016 the fast ice  
228 cover was relatively stable with a maximum area of  $\sim 6280$  km<sup>2</sup> in 2016. After 2016, the eastern portion of the fast ice,  $\sim 1200$   
229 km<sup>2</sup> in area, seasonally re-formed and broke out. The lowest extent in the MODIS record was in February 2019, when a slightly  
230 larger area (2000 km<sup>2</sup>) broke out. In late 2021 the outer portion broke out again, returning to the 2019 areal extent, and by  
231 early 2022 the extent was similar to the 2019 minimum (Supplemental Video. 1). Lateral rifts appeared in  $\sim 2016$  near the  
232 confluence of Scar Inlet Ice Shelf and Crane Glacier extending north and south from Cape Disappointment. Early assessments  
233 of the fast ice thickness in the Larsen B embayment near the oceanward ice front were 2.5 to 4 m (Scambos et al., 2017). In  
234 the inner embayment, altimetry data indicate a thickness of tens to hundreds of meters in areas of mélange containing fast ice  
235 and glacier tongue ice (Fig. 1; Fig. S1 and S2).



#### 236 4.1.2 Upstream glacier response to fast ice formation

237 During the 2011-2022 period of fast ice presence in the embayment, changes in the glacier extents and GNSS data suggests  
238 that the fast ice stabilized the Larsen B tributary glaciers and buttressed the Scar Inlet Ice Shelf, relative to the state prior to  
239 the fast ice occupation. This corroborates the findings of Christie et al. (2022). MODIS and Landsat images show that the  
240 glacier tongues readvanced into the embayment, and the fjords became a floating composite of glacier ice, large icebergs, and  
241 fast ice (hereafter, 'mélange'). The ice reached thicknesses of up to 320 m near the glacier tongue termini (inferred from  
242 freeboard estimates in Fig. 1). Crane Glacier's terminus and associated mélange advanced at  $\sim 1 \text{ km yr}^{-1}$  (11 km total) and the  
243 main trunk of the glacier thickened (Rott et al., 2018; Needell and Holschuh, 2023). The HGE floating tongue and mélange  
244 reformed into an ice-shelf-like feature with a central freeboard exceeding 40 m. HGE advanced approximately 20 km from  
245 February 2011 to January 2022, with the new floating mixed-ice-type area covering  $\sim 250 \text{ km}^2$ . Jorum Glacier advanced  $\sim 4.5$   
246 km over the same period, while Punchbowl Glacier only readvanced  $\sim 0.5$  km and did not create an extensive mélange or  
247 glacier tongue.

248  
249 GPS data from Scar Inlet Ice Shelf (Fig. 2) show an acceleration of ice shelf flow speed from installation of the GPS in early  
250 2010 to late 2012, followed by a cyclical variation in flow speed that varied by season. This indicates that the ice shelf was  
251 accelerating prior to the formation and thickening of the multi-year fast ice. From late 2012 onwards, the acceleration of the  
252 ice shelf was halted, and an annual cycle with faster flow during late summer-early autumn and a springtime minimum flow  
253 speed was observed. We infer that significant buttressing of the ice shelf by the fast ice mitigated the acceleration of the shelf.  
254 Moreover, the seasonal cycle of flow speed, with highest flow speed during mid-summer, is interpreted as an effect of seasonal  
255 weakening of the fast ice plate due to summer warmth (Pettit et al., in prep).



256

257 *Figure 2: Scar Inlet Ice Shelf ice flow speeds from AMIGOS GPS from 2010 to 2017. Blue line is the monthly mean, blue dots*  
 258 *are the weekly means, and green vertical lines are the daily means.*

259 **4.1.3 Multi-year fast ice break-up**

260 MODIS imagery shows that new narrow fractures started to form in the fast ice between 18 and 19 January 2022, widening  
 261 thereafter, and by 20 January the fast ice area was densely fractured and no longer coherent. By 21 January, floes derived from  
 262 the fast ice plate had drifted 9 to 16 km northeast into the Weddell Sea, exposing the tributary glacier fronts to open water (Fig.  
 263 1c). The fast ice floes continued to drift away, fully clearing the embayment by 8 February.

264

265 Pack ice began to reappear in the embayment in March 2022, but overall sea ice cover was not persistent through the next 12  
 266 months. Over the course of the late austral summer into the autumn and winter, MODIS images indicate overall sea ice cover  
 267 in the embayment varied in extent and apparent coherency. Open water conditions in the embayment and the area adjacent to  
 268 the AP and James Ross Island persisted through March 2022. Landfast ice did not form in the embayment during the southern  
 269 hemisphere autumn and winter 2022. In October 2022 the sea ice in the embayment varied in spatial extent, and began to  
 270 decrease significantly in November 2022, and by December 2022 there were minimal floating bergs or pack ice floes. From

271 January to March 2023 the embayment was devoid of floating ice and remained open ocean. However, by the end of March  
272 2023, pack ice and fast ice started to reform in the embayment.

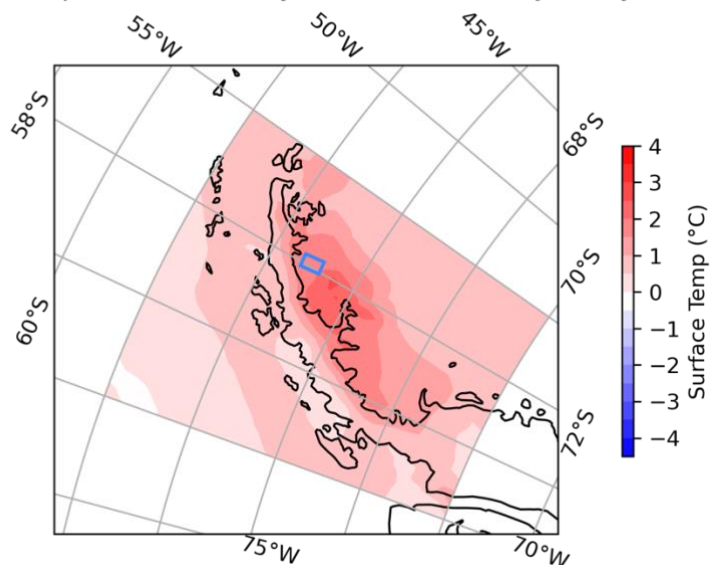
## 273 4.2 Potential Attributions of the 2021-2022 Fast Ice Breakout

### 274 4.2.1 Seasonal meteorological conditions

275 For November 2021 to January 2022, there is no substantial precipitation anomaly in our study area (Fig. S3A). The wind  
276 speed anomaly composites indicate a slightly higher than average wind speed during the 2021/2022 melt season, with  
277 December having the largest anomaly, primarily in the Bellingshausen Sea (Fig. S3B). The temperature anomaly over this  
278 period indicates the Bellingshausen Sea was slightly warmer ( $\sim 2^{\circ}\text{C}$ ) than the 1979 to 2022 climatological average, whereas  
279 the Larsen B embayment was up to  $4^{\circ}\text{C}$  warmer (Fig. 3).

280

#### Surface Temperature Anomaly November 2021 - January 2022

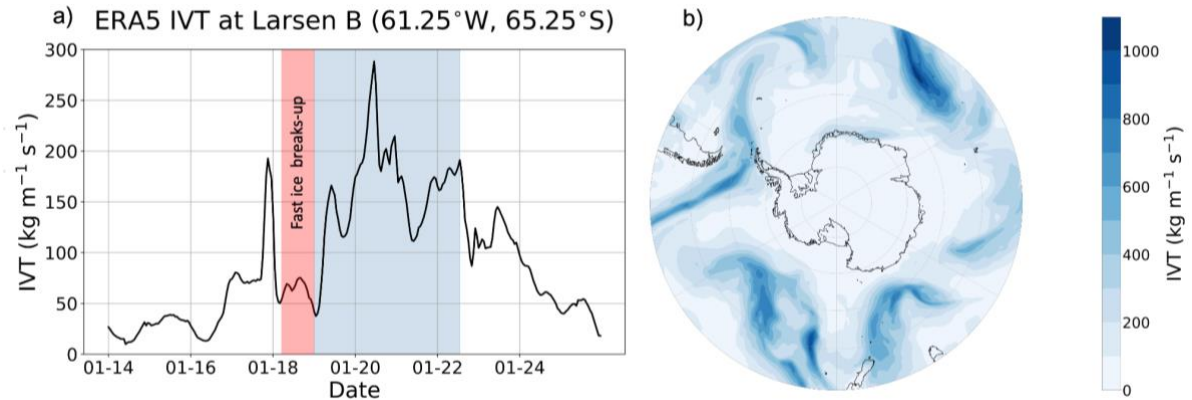


281

282 *Figure 3: ERA-5 surface air temperature anomalies around the Antarctic Peninsula. The blue box is the area of grid cells*  
283 *used for the foehn wind analysis (Fig. S4).*

284 We also looked at the January 2022 mean hourly values of several meteorological variables that indicate foehn wind events:  
285 temperature, windspeed, wind direction, relative humidity and net ablation for the Larsen B region (blue box, Fig. 3), (Fig.  
286 S4). Five identified foehn events occurred from 17 to 21 January 2022, two prior to the fast ice break-out, one during that  
287 event, and two after it. These events likely enhanced surface melting on the fast ice, potentially augmenting the break-up of  
288 the ice in the post-break-up days (19 and 21 January) and dispersing the fast ice floes northeastward in the following weeks.

289 Since ARs can be linked to foehn events and therefore to increased surface melting (Bozkurt et al., 2018), we also investigated  
290 AR occurrence in the period of the fast ice break-out event. A time series of IVT in the Larsen B region indicates that IVT  
291 associated with an AR event from the northwest begins to increase on 19 January and peaks on 20 January 11:00 UTC (Fig.  
292 4a and b; Wille et al., 2022). IVT remained high until 22 January, when the AR weakened and dissipated. This event occurred  
293 simultaneously as the series of foehn events from 19 to 22 January, suggesting the AR led to the foehn winds that occurred  
294 just after the initiation of the break-out.



295  
296 *Figure 4: a) time series of IVT for January 2022 at 65.25°S, 61.25°W. b) map of ERA-5 IVT in the southern hemisphere at*  
297 *11:00 UTC on 20 January 2022, during the peak IVT at Larsen B. The AR is identified as a long filament of high IVT that*  
298 *extends from the eastern Pacific across the Antarctic Peninsula and into the Atlantic Ocean. Red shading indicates the arrival*  
299 *of the swell and fast ice break-up. Blue shading indicates the duration of the AR event over Larsen B.*

#### 300 4.2.2 Surface melt

301 Figure 5 shows cumulative melt days for each melt season from 2012/2013 to 2020/2021 over the Larsen B multi-year fast ice  
302 and Scar Inlet Ice Shelf, derived from AMSR-E/2 passive microwave data. Fig. 5a shows a map of the grid cells used in the  
303 analysis, as well as cumulative melt days for the 2019/2020 season, 2020/2021 season (i.e. the two melt seasons preceding the  
304 break-up event), and the mean cumulative melt days for each season from 2012/2013 to 2020/2021. We do not include the  
305 2021/2022 melt day data in Fig. 5a because of the mid-season break out of the fast ice in that summer. Maps of cumulative  
306 melt days for all melt seasons are available in Fig. S5. Fig. 5b shows the spatially-averaged melt days over the study area, as

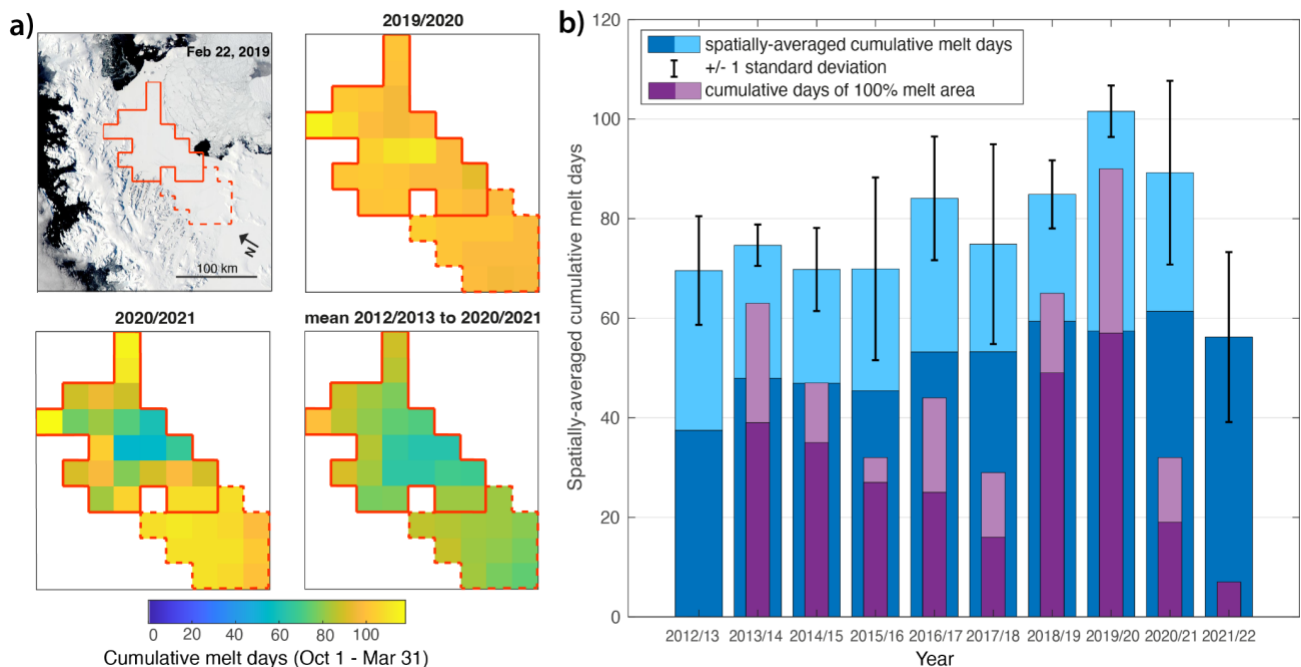
307 well as the cumulative days when the melt area was 100% of the study area, for nine melt seasons leading up to the break-up  
308 event, as well as the melt season with the fast ice break-out (2021/2022).

309

310 The 2021/2022 season did not have a particularly long or spatially more extensive melt season relative to the previous nine  
311 melt seasons. Of the years studied, 2019/2020 had both the longest melt season and the one with the highest number of days  
312 with 100% melt area; nonetheless the fast ice survived this season, as well as the preceding high-melt years.

313

314 In addition to our analysis of passive microwave data (above), which may indicate the presence of surface meltwater ponding  
315 (e.g. Picard et al., 2022), we also analyzed optical satellite images for evidence of surface meltwater ponding. Landsat 8 images  
316 in November and December 2021 show the surface of the fast ice was extensively covered with melt ponds (Fig. S6). However,  
317 by January 2022, the surface melt ponds on the fast ice appeared to have refrozen, and melt pond extent was reduced (Fig. S6).



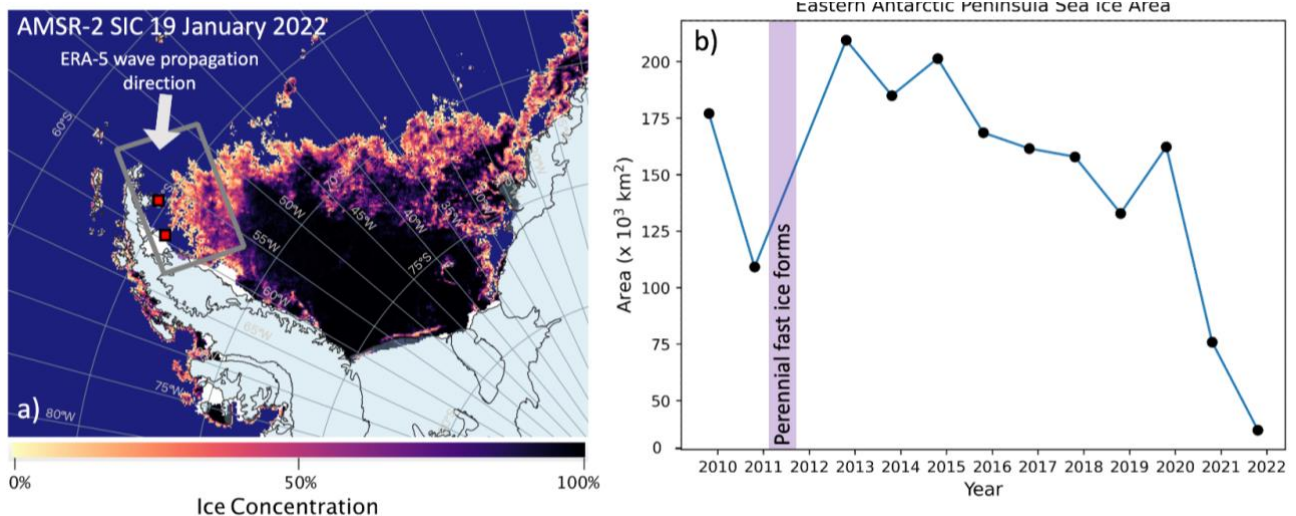
318

319 *Figure 5: Cumulative melt days derived from AMSR-E/2 passive microwave melt data. a) Cumulative melt days over the fast*  
320 *ice area in the Larsen B embayment (area within solid red lines) and over the Scar Inlet Ice Shelf (area within dashed red*  
321 *line) for the 2019/2020 and 2020/2021 melt seasons, and the mean from 2012/2013 to 2020/2021. b) Spatially-averaged melt*  
322 *days (blue shades) and cumulative days of 100% melt area (purple shades) over just the Larsen B embayment fast ice (solid*  
323 *red lines in panel a) from 2012/2013 to 2021/2022. The dark purple and dark blue bars show cumulative melt days from just*  
324 *1 October through 18 January (i.e. the data available for the 2021/2022 season), and the light purple and light blue bars show*  
325 *cumulative melt days from 1 October through 31 March.*

### 326 4.2.3 Regional Sea ice Cover

327 Figure 6a displays a mapping of sea ice concentration from AMSR-E/2 data in the Weddell Sea on 19 January 2022. Fig. 6b  
328 shows a time series of overall sea ice area (concentration that is greater than 15% multiplied by area of pixel) for the date of  
329 19 January for each year from 2010 to 2022 in a selected region (gray box in Fig. 6a; 2011/2012 did not have AMSR-E/2  
330 sensor data on this date; MODIS imagery shows extensive sea ice cover in the Larsen B fast ice front area through this time).  
331 The selected region represents a potential ocean swell corridor leading to the Larsen B embayment from 2010 to 2022 (see  
332 Section 5.2; also Teder et al., 2022). For the 8-year period (2013 to 2020 inclusive) the overall sea ice area in this region of  
333 the northwest Weddell Sea was over 125,000 km<sup>2</sup> (>50% of the box area). In 2011, sea ice area was just 100,000 km<sup>2</sup> on 19  
334 January; however, we note that the fast ice formed later in this year (March). The overall sea ice area dropped in 2021 to 75,000  
335 km<sup>2</sup>, and in 2022 its area was just below 40,000 km<sup>2</sup>. As Fig. 6a shows, a corridor is present along the eastern side of the  
336 Peninsula in January 2022, which opened on ~8 January 2022 according to the MODIS and AMSR-E/2 record. This pathway,  
337 which allows for wave action to access the front of the Larsen B fast ice, had not been present since the fast ice's formation in  
338 2011 (Figs. 6b and S7).

339

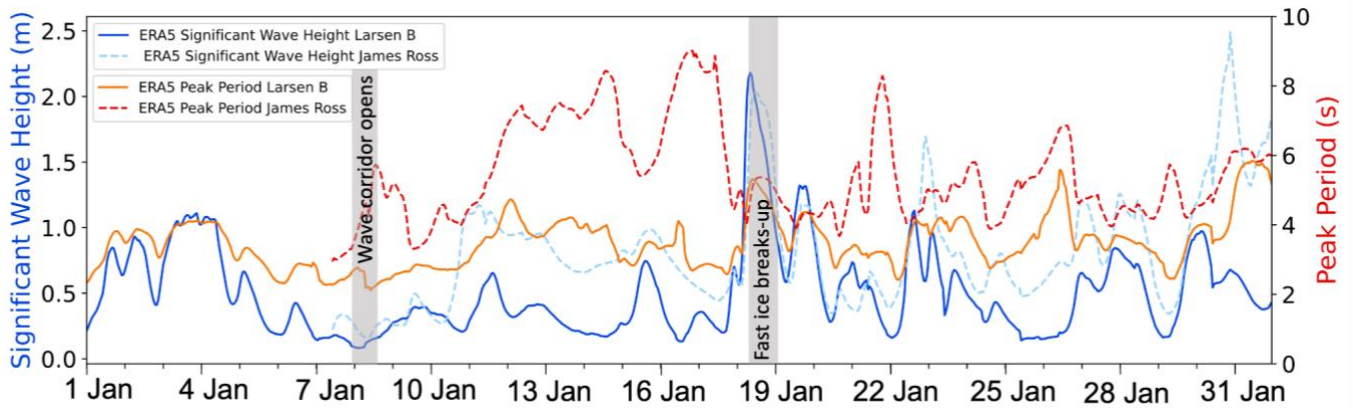


340

341 *Figure 6: a) Pack sea ice concentration and distribution map on 19 January 2022 from AMSR-2 data (Spren et al., 2008).*  
342 *Small red squares show the location of the ERA-5 wave height grid cells (Fig. 7). The gray box is the region selected for the*  
343 *overall sea ice area in 6b. The white arrow denotes the wave propagation direction on 19 January ERA-5 data. b) Overall sea*  
344 *ice area (concentration in each grid cell multiplied by the grid cell area) from AMSR-E and AMSR-2 data in the corridor*  
345 *region of the NW Weddell Sea for 2010 to 2022. Error in sea ice concentration according to Spren et al. (2008) is ~7%.*  
346 *Purple vertical shading indicates the time period of fast ice formation.*

347 **4.2.4 Wave action**

348 Examining both ERA-5 and WaveWatch-III wave data, the first large swell able to pass through the open-ocean (sea ice-free)  
349 corridor and reach the Larsen B fast ice edge occurred on 18 and 19 January (Figs. 7 and S8). In the early hours (UTC) of 18  
350 January 2022, the significant wave height averaged ~0.1 m in the selected grid cell region. By the afternoon on 18 January the  
351 average wave height rose steeply to a maximum of 1.75 m near Larsen B and to over 2 m near James Ross Island ~150 km to  
352 the northeast (red boxes, Fig. 6). Simultaneously, the peak wave period increased to ~5 s, indicating a wavelength equivalent  
353 to ~40 m. The wave propagation direction was bearing  $\sim 250^\circ \pm 25^\circ$  through this period, similar to the orientation of the open  
354 corridor in the pack ice. There were no events in November or December 2021 that included both a long peak period and a  
355 high significant wave height (and in any case, pack ice damped wave propagation in the region until ~8 January). Both months  
356 have peak periods consistently less than 6 s and wave heights below 1.4 m (Fig. S8 and S9). Furthermore, there were no other  
357 times during January 2022 when the wave swell had both a long peak period and high significant wave height (Fig. 7). Abrupt  
358 shifts in peak period and significant wave height (see Methods) are evident when the wave corridor opens near James Ross  
359 Island (gray band 8 Jan 2022) and when the event occurs (gray band 18 Jan 2022), as well as when the wind direction changes  
360 (Fig. S4).  
361



362  
363 *Figure 7: ERA-5 significant wave height (blue) and peak period (red) for both the Larsen B area (solid lines) and near James*  
364 *Ross Island (dashed lines) during January 2022. The red and dark red lines and the blue and light blue lines correspond to*  
365 *the peak period and significant wave height, respectively. The opening of the wave corridor and fast ice break-up are denoted*  
366 *by the gray vertical bands.*

## 367 **4.3 Initial glacier response to fast ice break-out**

### 368 **4.3.1 Retreat of glacier fronts**

369 Four glaciers along the Larsen B embayment coast responded almost immediately to the fast ice break-out. Crane and Jorum  
370 Glaciers exhibited similar responses, losing most of their floating ice tongues within days of the fast ice breakout (Fig. 8a) and  
371 calving a number of large (several km<sup>2</sup>) full-thickness tabular icebergs. Once the floating tongue portion was removed, both  
372 glaciers underwent buoyancy-driven calving and a tidewater-style retreat at their grounding zones, indicated by the presence  
373 of toppled icebergs in optical images and high-backscatter iceberg surfaces in Sentinel-1 data. Scattering intensity is related to  
374 surface roughness as well as how much melt has affected the surface of the berg; freshly toppled cold bergs will have a brighter  
375 surface, whereas tabular bergs that have been exposed to surface melt will display a decreased backscatter intensity (Young et  
376 al., 1998). Punchbowl Glacier began calving in a style that appears to be buoyant full thickness calving (Murray et al., 2015),  
377 indicated by toppled dark blue icebergs. Unlike Crane, Jorum, and HGE, Punchbowl did not readvance into the embayment  
378 during the fast-ice occupation. Hektoría and Green Glacier retained a 13 km extended thick (greater than 300 m) floating  
379 tongue after the immediate break-out, until March 2022. However, at this point their floating ice areas also underwent full-  
380 thickness tabular calving with occasional toppled icebergs (Fig. 8). From April to October 2022 the ice fronts were relatively  
381 stable, but rapid retreat reinitiated in November 2022. The calving style resembled tidewater glacier retreat for grounded ice  
382 with buoyant calving, similar to the Röhss Glacier response from the loss of the Prince Gustav Ice Shelf (Glasser et al., 2011)  
383 or calving regimes at Helheim Glacier, Greenland (Murray et al., 2015).

384

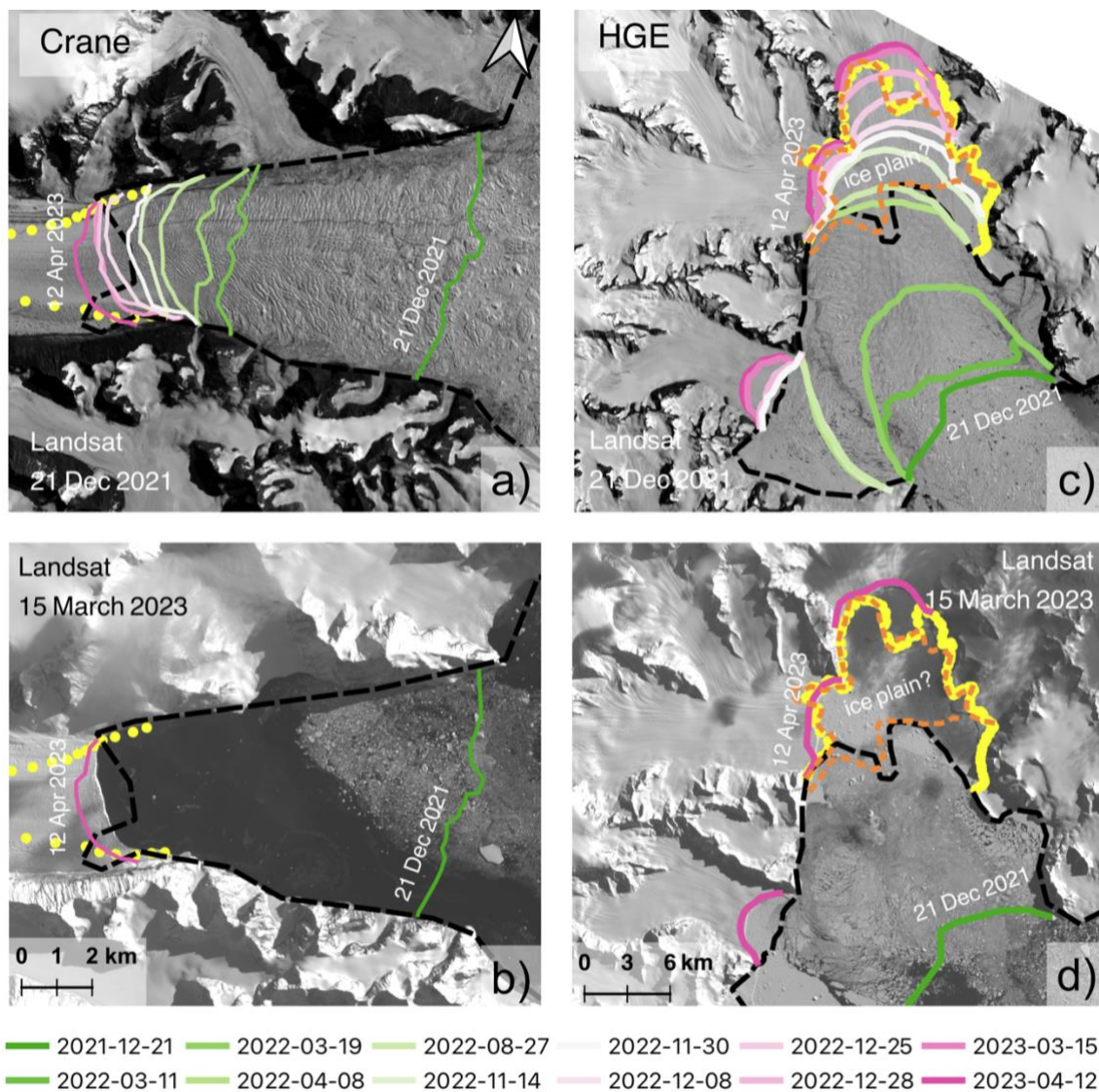
385 In the weeks and months following the fast ice break-up, Crane, Jorum, and Punchbowl glaciers continued to retreat. By 8  
386 February 2022 the Crane Glacier floating front (defined here as the limit of contiguous ice > 100 m in thickness; consistent  
387 with Needell and Holschuh, 2023) had retreated more than 6.5 km and was still calving large tabular bergs (several km<sup>2</sup> and >  
388 300 m thick, based on WV DEMs; Fig. 8a). From 8 February until 11 March 2022 only 400 to 800 m of retreat occurred. Crane  
389 continued its episodic periods of retreat of several hundred meters at a time throughout the 2022-2023 summer season (Fig.  
390 8a). Its retreat totalled ~11 km, of which possibly 1 to 2 km was grounded ice using this study's grounding zone or no grounded  
391 ice using Rott et al. (2018)'s, 2016 grounding line (Fig. 8b). Similar to Crane in calving style, the Jorum Glacier main trunk  
392 lost ~5 km of floating ice and its (former) tributary branch glacier lost ~6 km. Punchbowl Glacier, in contrast, has only lost a  
393 few hundred meters of its ice front as of May 1 2023.

394

395 Hektoría and Green Glacier responded to the fast ice break-out in later months. Hektoría Glacier had an extended thick (> 300  
396 m) floating tongue that persisted until 12 to 17 March 2022, when it retreated ~7 km (Fig. 8c). From 26 to 30 March, Hektoría's  
397 floating tongue retreated another ~6 km, exposing an arcuate ice front. From April 2022 until August, Hektoría's ice front  
398 retreated ~1 km. This retreat is inferred to be the start of the grounded ice retreat based on a change in calving style and surface  
399 morphology of the upstream ice. For all of September and October Hektoría's front did not change. Hektoría retreated ~3 km



400 by 14 November and another 1.2 km by 30 November 2022. In December 2022, Hektoria underwent another series of retreats  
 401 totaling ~4 km. From 17 January to 15 March 2023, another ~1.5 km retreat into the fjord occurred, and Hektoria is still  
 402 actively retreating as of April 2023 and has retreated a total of ~25 km, of which ~10 km may have been grounded ice using  
 403 this study's grounding zone or 1 to 5 km of grounded ice using Rott et al., (2018)'s 2016 grounding line (Fig. 8d). Green  
 404 Glacier has also retreated substantially but not as far into its fjord. Following a similar timeline to Hektoria, Green has retreated  
 405 ~18 km total.  
 406



407  
 408 *Figure 8: Yellow points are Rott et al., 2018's grounding zone, black dashed lines are this study's inferred grounding zone,*  
 409 *orange dotted lines are Tuckett et al., 2020's grounding zone and ice plain location; a) Crane Glacier retreat fronts from*

410 *November 2021 to April 2023, length scale is the same as panel b; b) Crane Glacier with pre-break out terminus position and*  
411 *April 2023 terminus position; c) HGE system retreat fronts from November 2021 to April 2023, length scale is the same as*  
412 *panel d; d) HGE system with pre-break out terminus position and April 2023 terminus position. For a) and c) the background*  
413 *is a Landsat 8 image from 21 November 2021, and for b) and d) the background is a Landsat 9 image from 15 March 2023.*

#### 414 **4.3.2 Glacier centerline speed changes**

415 Initial ice flow speed profiles along near-centerline tracks of Crane, Jorum, Green and Hektoría glaciers all show an increase  
416 in speed of various magnitudes since the fast ice break-out event. For all the glaciers besides Punchbowl, the floating portions  
417 increased in speed dramatically immediately after the break-out event while the grounded portion of the glaciers took many  
418 months to be affected, according to this study's grounding zone estimation (Fig. 9a-c; gray shaded bands on profiles and dashed  
419 white lines on insets). Additionally, the observed speed profiles in the 26-month period (January 2021 to March 2023) show  
420 far less local variability upstream of our inferred grounding line.

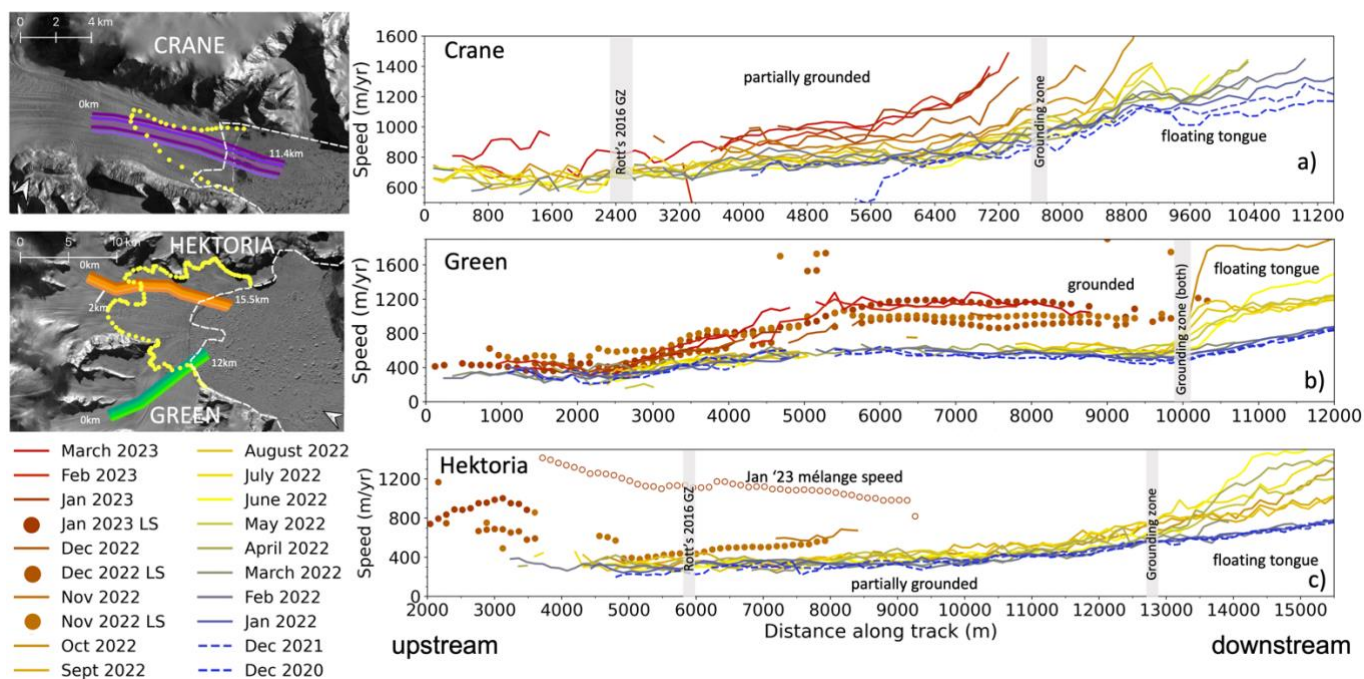
421  
422 The Crane Glacier tongue accelerated and extended along-flow immediately after the event leading to an increase of speed  
423 from 1000 m yr<sup>-1</sup> to 1300 m yr<sup>-1</sup> within the first two months (Fig. 9a; light blue to yellow-green solid lines). The grounded  
424 portion of Crane Glacier responded in the months following. By November 2022 the grounded ice speed increased from 800  
425 to 900 m yr<sup>-1</sup> (Fig. 9a; yellow to dark-yellow solid lines) and by March 2023 the speed was 1200 m yr<sup>-1</sup> (Fig. 9a; red solid  
426 lines). Crane Glacier is still undergoing retreat and acceleration as of March 2023.

427  
428 Jorum Glacier did not experience as dramatic a change in speed after the event. Jorum Glacier has three flow speed sections:  
429 the upper glacier was slow-moving at 100 to 200 m yr<sup>-1</sup>, the glacier's steep portion accelerated to 500 m yr<sup>-1</sup> over a distance  
430 of 1.5 km, and the lower glacier flowed at ~475 m yr<sup>-1</sup> prior to the break-out (Fig. S10). By November 2022, this lower section  
431 increased in speed by ~75 to 100 m yr<sup>-1</sup>, and has remained at ~550 m yr<sup>-1</sup> as of March 2023 (Fig. S10). Jorum Glacier's floating  
432 tongue quickly calved away after the event so the floating icebergs and loose mélange were not tracked for speed.

433  
434 The HGE system experienced significant changes after the break-up of the fast ice. While the floating portion of the system  
435 did not experience speed changes immediately after the fast ice loss (Fig. 9a-c; January to March 2022; light blue to yellow-  
436 green solid lines). The floating tongue was removed by April 2022 leaving only grounded ice, according to this study's  
437 grounding zone estimation. The mélange speed is tracked when the mélange is cohesive (solid lines downstream of this study's  
438 grounding line from April 2022 onwards), reaching ~1500 (Hektoría) and 1700 m yr<sup>-1</sup> (Green) by October 2022.

439  
440 Speed changes occurred in the lower trunk areas of both Green and Hektoría glaciers. Green Glacier increased from ~500 m  
441 yr<sup>-1</sup> prior to fast ice break-up to 1150 m yr<sup>-1</sup> by January 2023. Green Glacier's SAR-derived and Landsat-derived ice speeds  
442 for December 2022 and January 2023 agree with the general trend (Fig. 9b; light brown and brown solid lines). Hektoría

443 Glacier's Landsat-derived ice speeds show a velocity increase 10 km upstream of the grounding line from September 2022 to  
 444 January 2023 from 400 to 900 m yr<sup>-1</sup> (Fig. 9c; light brown and brown solid lines). Both Green and Hektoria are still undergoing  
 445 retreat and acceleration as of March 2023.

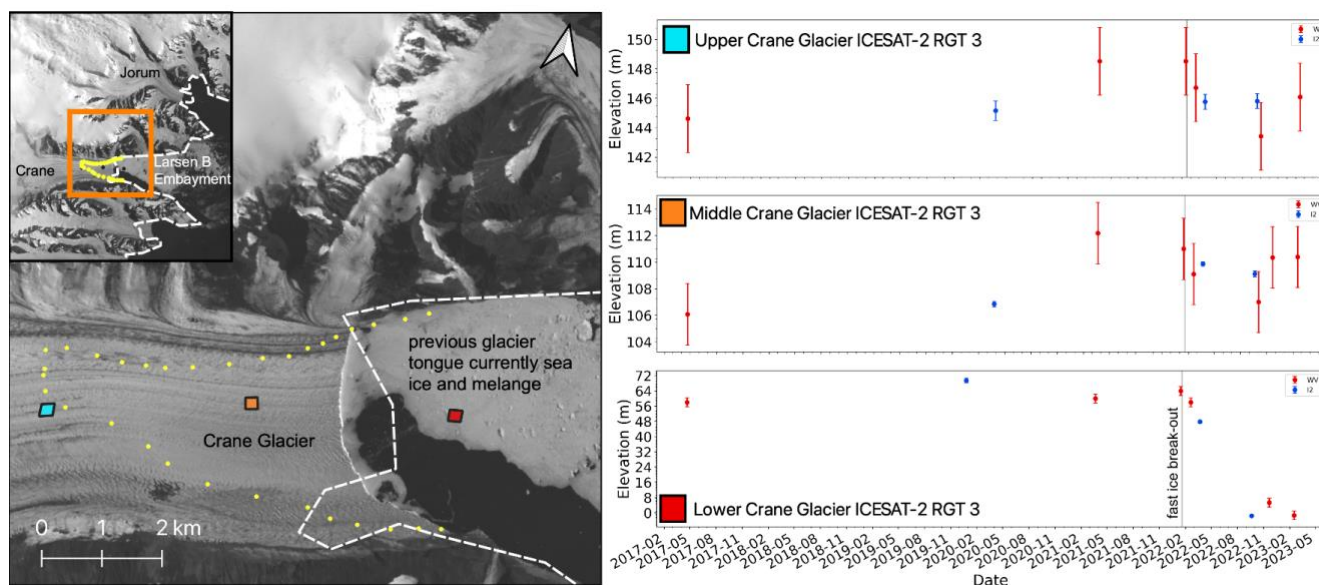


446  
 447 *Figure 9: Monthly averaged ice flow speeds along the IceBridge flight centerlines, derived from Sentinel-1 speckle tracking*  
 448 *from Alaska Satellite Facility HYP3-pipeline, solid-colored lines. Image pair flow speeds from Landsat imagery (using*  
 449 *PyCorr) are indicated by colored solid dots. Gray bands on profiles and dashed white line on image insets show inferred*  
 450 *grounding zones, with the Rott et al. (2018) grounding zone of 2016 as yellow points on insets. a) Crane Glacier velocity*  
 451 *profile. b) Green Glacier velocity profile. c) Hektoria Glacier velocity profile. The open circles represent the mélange speed*  
 452 *from the January 2023 Landsat velocity data. The along-track distances are set at an arbitrary point well upstream of each*  
 453 *glacier's grounding zone. Blue dashed lines are reference years Dec 2021 and Dec 2020, prior to break-out. Background*  
 454 *image is a Landsat 9 image from 06 October 2022.*

### 445 4.3.3 Elevation changes

456 We used ICESat-2 altimetry and WV-1, -2, and -3 stereo-image DEMs to assess elevation changes of the Larsen B embayment  
 457 glaciers from 2017 to present. For each glacier, we evaluated three reference points along the near-centerline to these changes.  
 458 Lower Crane Glacier (red box, Fig. 10) may have thinned by up to 16 m immediately after the fast ice break-out, however the  
 459 trend is incomplete due to the glacier's rapid retreat and calving. This abrupt thinning may have been a consequence of a  
 460 change in calving style near the front, e.g., listric faulting in the ice (e.g., Parizek et al., 2019). Our trend for the middle and  
 461 upper section of Crane (orange and blue box, Fig. 10) shows thickening from 2017 to 2022, consistent with Needell and

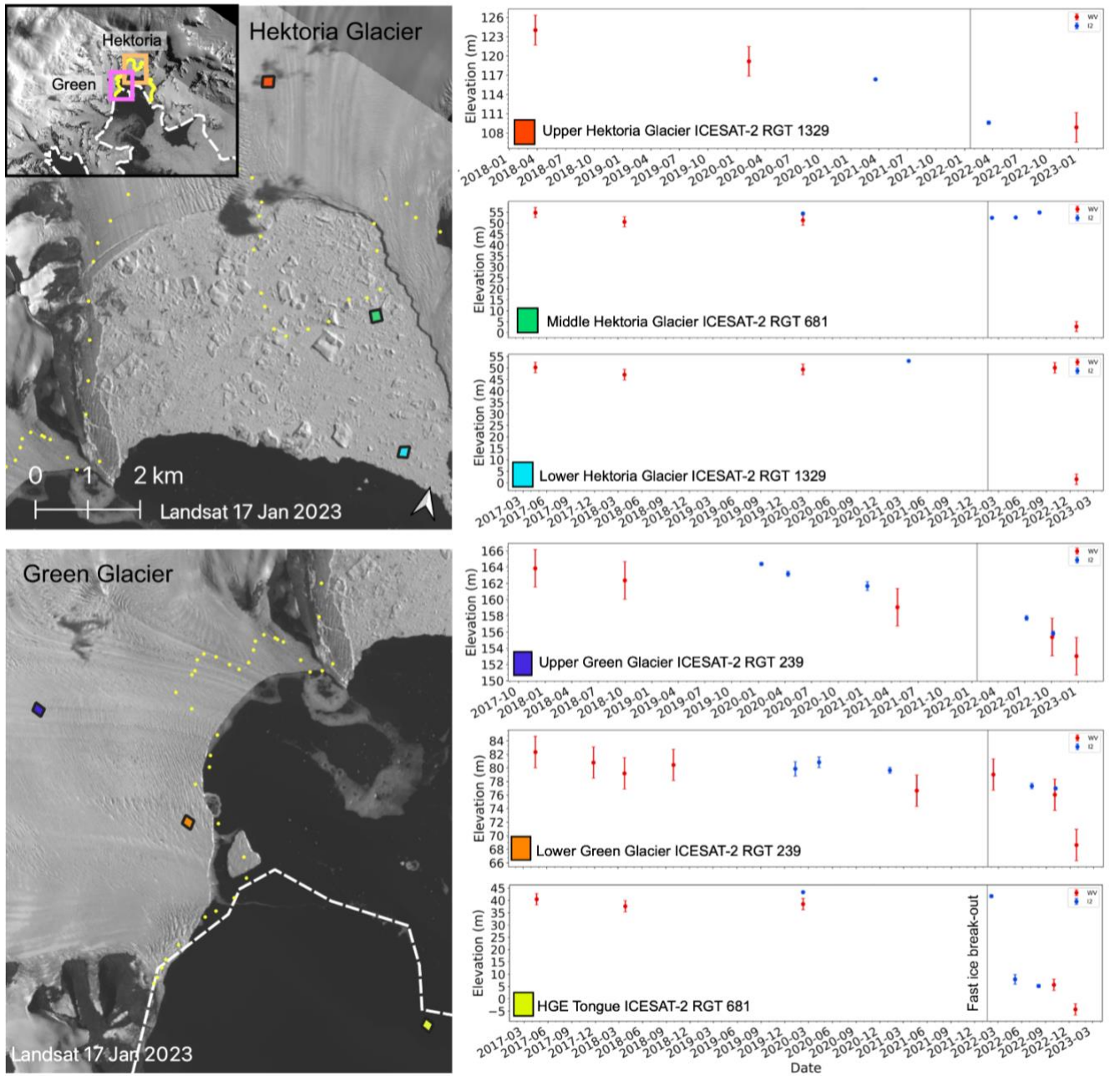
462 Holschuh's (2023) findings. Thinning may have now begun in those regions, however the data are inconclusive, as the thinning  
 463 is only 1 to 3 m as of February 2023, which is within the measurement error and surface roughness variations on the glacier.  
 464 Jorum and Punchbowl glaciers show very variable results as well (Fig. S11).  
 465



466  
 467 *Figure 10: Crane Glacier near-centerline elevation changes through time. Background image is from Landsat 9 17 January*  
 468 *Landsat. The time series plot corresponds to the area of the box of the same color. The gray band indicates the date of*  
 469 *the fast ice break-out event. Note the different vertical scales on the figure.*

470 The HGE system shows thinning in various regions and rapid calving and retreat in the elevation data.. Figure 11 (yellow box)  
 471 shows the HGE system floating tongue freeboard as 40 m, which is consistent with a ~320 m glacier thickness, assuming  
 472 hydrostatic equilibrium. After the break-out event, icebergs (which we define as ice with >5 m freeboard) are present in the  
 473 fjord until the open ocean period (December 2022). Lower Hektoria Glacier lacks elevation change data points from the start  
 474 of the collapse, simply because the downstream-most regions calved and drifted away before a repeat elevation measurement  
 475 could be acquired (blue and green boxes; Fig. 11). The upper portion of Hektoria (dark orange box; Fig. 11) appears to have  
 476 thinned since early 2018 (or prior). Minimal thinning occurred from April 2022 to late December 2022. As of 6 April 2023,  
 477 this portion of the glacier is just 400 m upstream from the rapidly retreating glacier terminus and is unlikely to remain intact  
 478 for further measurements. Both the lower and upper Green Glacier (orange and blue boxes, respectively; Fig. 11) show strong  
 479 thinning above the level of surface variability from 2017-present. Lower Green Glacier thinned ~11 m between March 2022  
 480 to late December 2022, going from 79 m to 68 ±2.3 m. Upper Green Glacier thinned ~9 m between January 2021 to late  
 481 December 2022, going from 162 ±0.5 m to 153 ±2.3 m. There are no data available between January 2021 and July 2022, so

482 the initiation of thinning of the glacier is uncertain. However, from July 2022 until late December 2022, ~5 m of the total 9 m  
 483 of thinning occurred.  
 484



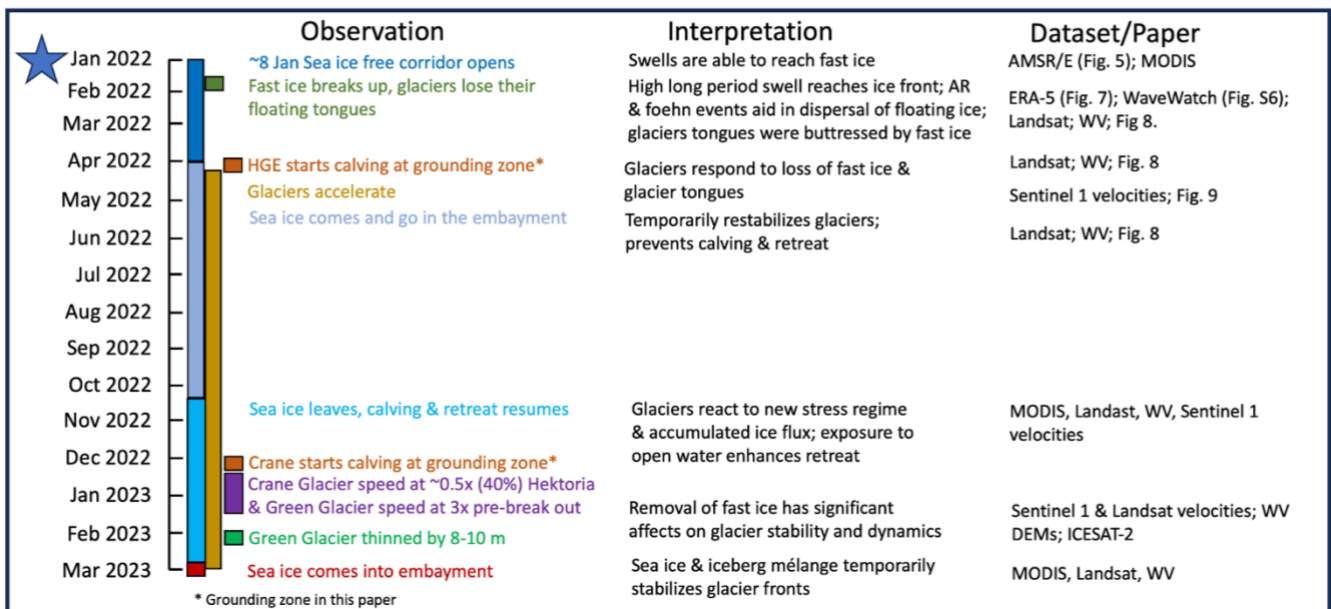
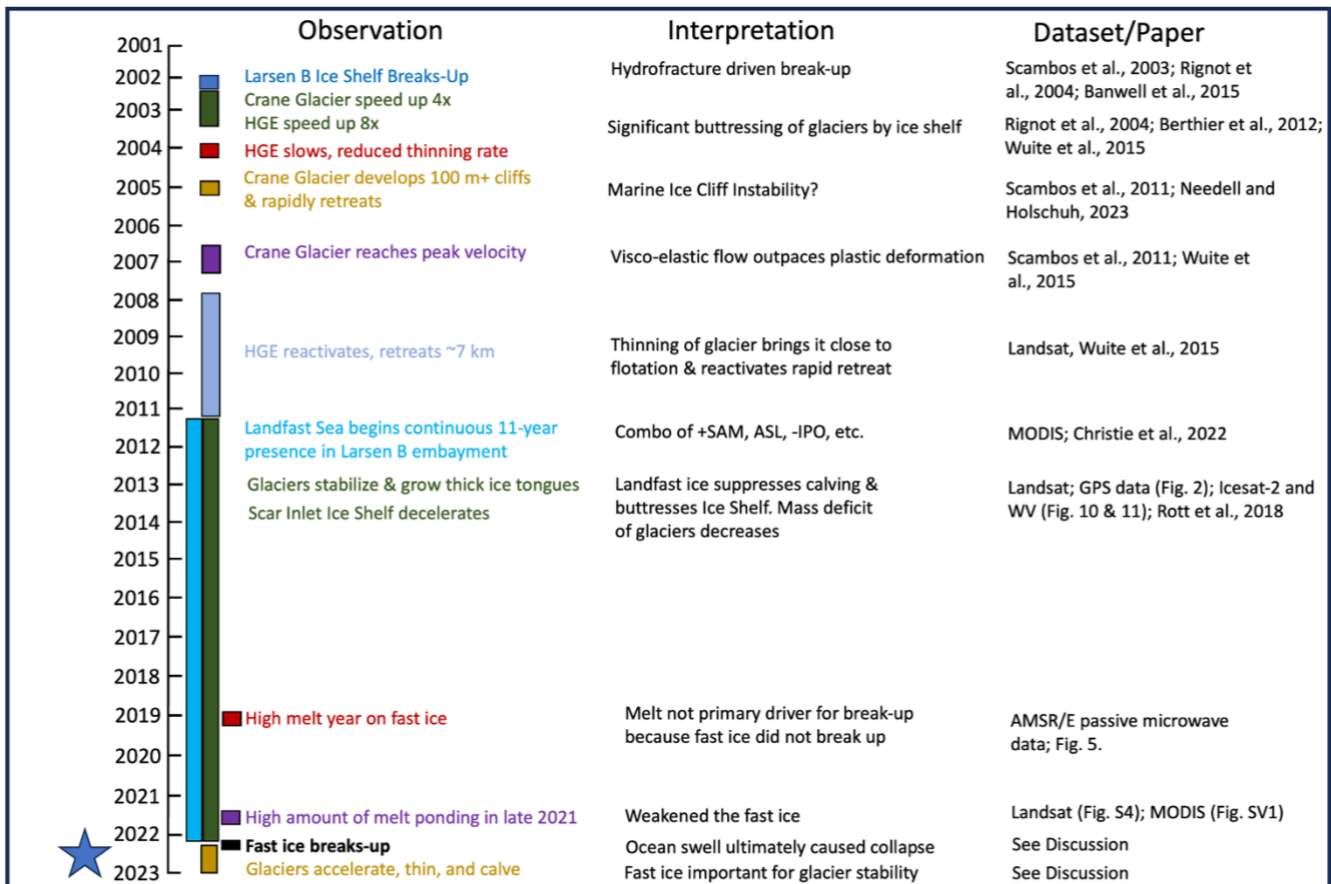
485  
 486 *Figure 11: Hektoria and Green Glacier system elevation changes through time. Background image is from Landsat 9 17*  
 487 *January 2023 Landsat, yellow points indicate the Rott et al. (2018) 2016 grounding zone and white dashed line is the grounding*

488 *zone inferred in this study. The pink box in the study area inset is the area depicted for Green Glacier and the orange box is*  
489 *Hektoria Glacier. The time series plot corresponds to the area of the box of the same color. The gray band indicates the date*  
490 *of the fast ice break-out event.*

## 491 **5 Discussion**

492 Figure 12 summarizes the chronology of events in the 22-year period from 2001-2023 of the Larsen B embayment and the  
493 tributary glaciers. We document the changes that have occurred during the two break-out events and how the glaciers and the  
494 Scar Inlet Ice Shelf have responded to those events. Below we discuss the conditions and aftermath of the 2022 event in light  
495 of our findings and related literature.

496



497

498

Figure 12: Schematic of the chronology of events from 2001-2023 of the Larsen B embayment region discussed in the text.

## 499 **5.1 Meteorological Conditions and Modes of Atmospheric Variability**

500 The AP climate is influenced by several large-scale modes of atmospheric variability. These patterns are drivers of the  
501 formation and demise of pack ice, fast ice, the mass balance and stability of the glaciers and ice shelves. Climate patterns and  
502 variability are driven by several modes with a variety of time scales, e.g., the Interdecadal Pacific Oscillation (IPO) at 10 to  
503 30 years and SAM phase oscillations, changing on the scale of weeks to months. The IPO was in a negative phase from 2000  
504 to 2014, favoring an increase of overall sea ice extent at  $\sim 0.57 \pm 0.33 \times 10^6 \text{ km}^2$  per decade (Meehl et al., 2016). Additionally,  
505 slightly cooler conditions around the AP in the 2010s limited the area of melt ponding on the Scar Inlet Ice Shelf and the  
506 northern Larsen C (Cape et al., 2015; Bevan et al., 2018). This situation paired with intensified cyclonic circulation in the  
507 Weddell Sea (Christie et al., 2022), which may be broadly favorable for the formation of the Larsen B embayment fast ice and  
508 advancement of the glacier tongues (Fig. 12), yet due to local variability it can be difficult to pinpoint its exact drivers in a  
509 specific season. It appears the IPO reversed in 2015/2016 but that remains to be confirmed (Li et al., 2021). The SAM index  
510 has been trending toward more frequent periods of positive phase for many decades (Kwon et al., 2020; Li et al., 2021). A  
511 positive SAM is generally associated with a deepening of the Amundsen Sea Low, which subsequently enhances northwesterly  
512 flow across the AP, bringing warm air masses and an increase in foehn events into this region (Li et al., 2021; Turner et al.,  
513 2022). A positive SAM is also correlated with AR events, due to enhanced moisture fluxes towards the Antarctic Peninsula  
514 and a more easterly storm track, which can increase warming on the eastern (lee) side of the Antarctic Peninsula during AR-  
515 driven foehn events (Wille et al., 2021; Shields et al., 2022; Wille et al., 2022). Strong westerly winds increase pack ice drift  
516 eastward and northward, exposing the AP's eastern coast and ice fronts to open ocean. This may have caused the low sea ice  
517 cover in the Weddell Sea in summer 2021/2022 and lack of pack ice in the corridor region in January 2022 (Turner et al.,  
518 2022).

519  
520 We found that the climate of the Larsen B region was anomalously warm from November 2021 to January 2022. However,  
521 despite the climate being warmer, the number of melt days, and mean areal extent of melt, over the fast ice derived from the  
522 passive microwave data in the 2021/2022 season were not a record (Fig. 5). According to the optical imagery, melt ponds were  
523 evident in Landsat 8 satellite images mainly in November and December 2022, however the areal extent of melt ponds in the  
524 Larsen B region declined prior to the fast ice break-out event in late January 2022 (Fig. S6). These observations suggest that  
525 neither surface melting, nor related hydrofracturing of pre-existing melt ponds in the thick glacier tongues, were a direct cause  
526 of the 19 January fast ice fracturing or the subsequent break-up, although they do point to a warmer (and likely weaker) fast  
527 ice cover at mid-summer of 2021/2022.

528  
529 The low overall sea ice concentration and westerly winds from a deep Amundsen Sea Low led to an open water corridor  
530 between the pack ice and the eastern coast of the AP (Turner et al., 2022). This led to the region in front of the Larsen B having  
531 the lowest total overall sea ice area for the date in 13 years (2010-2022; Fig. 6). In February 2021, there was a smaller open  
532 corridor, however, the area was not as wide as in early January 2022 and did not create an unobstructed ice-free lane to Southern



533 Ocean swell. With low sea ice damping, ocean swell events could impact the eastern fast ice and coastal areas; these have been  
534 shown to destabilize fast ice and ice shelves (Crocker and Wadhams 1989; Langhorne et al. 2001; Banwell et al., 2017; Massom  
535 et al., 2018; Teder et al., 2022). However, swell events in February 2021 were low amplitude or proceeded from the coast to  
536 the northeast, i.e. likely driven by foehn events.

## 537 **5.2 The fast ice break-out event**

538 Despite high temperatures and surface melt and meltwater ponding (Scambos et al., 2003; Banwell et al., 2013), alongside  
539 thinning due to both basal melting and surface melting (Adusumili et al., 2018; Smith et al., 2020), known to be primary drivers  
540 of ice shelf collapse, our analysis shows that the Larsen B multi-year fast ice persisted through warm and high melt years (e.g.,  
541 2019/2020; Bevan et al 2020; Banwell et al., 2021) without breaking up. Until the 2021/2022 melt season, the absence of a  
542 large sea ice-free corridor prevented high ocean swells from the northeast from reaching the fast ice (Fig. 12). Long period  
543 ocean swells, such that the wavelength is substantially greater than the ice thickness, can expose ice shelves and fast ice to  
544 flexural strains (Crocker and Wadhams, 1989; Langhorne et al. 2001; Banwell et al., 2017; Massom et al., 2018). In our case,  
545 the fast ice was several meters thick, wave height was nearly 1.75 m, and the wave period at the time of the event was 5 to 6  
546 s, corresponding to wavelengths of order of 40 m (Fig. 7). The resulting strains can weaken the outer margins of the fast ice or  
547 ice shelf through plate-bending and fracturing. As the outer margin breaks, the stress is redistributed within the fast ice, possibly  
548 initiating further fractures within the ice (Massom et al., 2018). The fast ice was potentially preconditioned to break-up by the  
549 rifts that were open near the confluence of the Crane Glacier tongue and Scar Inlet Ice Shelf, however, contrary to Sun et al.  
550 (2023) we attribute the break-up to the long period, high-amplitude swell that came from the northeast through the open sea  
551 ice corridor. This order of events and ultimate cause of break-up is similar to what was proposed in Gomez-Fall et al. (2022)  
552 for the collapse of the Parker Ice Tongue.

553  
554 The rapid removal of the fast ice fragments from the embayment coincides with the presence of foehn winds that were likely  
555 caused by an AR event. Recently, ARs and AR-triggered foehn events have been linked to the collapse of ice shelves due to  
556 their ability to cause extreme surface melting and subsequent hydrofracture (Laffin et al., 2022; Wille et al., 2022). Here, we  
557 found that foehn events happened prior to, during, and after the January 2022 Larsen B wave event. We cannot rule out the  
558 possibility that these foehn events may have sufficiently increased melting on the thick glacier tongues to cause  
559 hydrofracturing, which may have acted to further fracture the fast ice and facilitate break-up. As a secondary driver, the winds  
560 likely hastened the removal of the floating ice or helped create the open corridor for wave entry to reach the ice fronts. These  
561 findings parallel that of Massom et al. (2018) who attributes the Larsen B Ice Shelf break-up in 2002 to the removal of sea ice  
562 due to westerly/north westerly winds that not only enabled an ocean swell to reach the ice shelf but also helped to quickly  
563 evacuate large icebergs and mélange out of the embayment. Additionally, the AR and foehn events in January 2022 may have  
564 affected sea surface slope. It is possible that a sea surface sloping oceanward gravitationally promoted calving and removal of  
565 the floating ice, similar to the calving of large icebergs off the Amery Ice Shelf in 2019 (Francis et al., 2021), the Brunt Ice

566 Shelf in 2021 (Francis et al., 2022), and Larsen D in 2020 (Christie et al., 2022). We suggest further research to investigate the  
567 presence of cyclone(s) and the sea surface slope during the time of the break-up event.

### 568 **5.3 The initial glacier response**

569 After the break-up of the ice shelf in 2002, the presence of fast ice significantly affected the tributary glaciers' dynamics,  
570 providing sufficient backstress that suppressed calving and permitted the tributary glaciers to form thick ice tongues and  
571 readvance into the embayment during 2010 to 2022 after the initial break-up in 2002 (Fig. 2; Needell and Holschuh, 2023),  
572 corresponding to an Eastern Antarctic Peninsula-wide ice front advance discussed in Christie et al. (2022). Rigid mélange  
573 and/or fast or pack ice can stabilize rifts (Larour et al., 2021), and can allow ice shelves, tidewater glaciers, or floating glacier  
574 tongues to advance, as has been seen in Greenland (Moon et al., 2015), the Parker Ice Tongue (Gomez-Fell et al., 2022), the  
575 Cook West Ice Shelf (Miles et al., 2018), and other areas (Reeh et al., 2001; Massom et al., 2010; Cassotto et al., 2015; Banwell  
576 et al., 2017). During the 2010 to 2022 period of the occupation of the Larsen B multi-year fast ice, the tributary glaciers Crane,  
577 Hektor and Green readvanced and decelerated (Rott et al., 2018) and the Scar Inlet Ice Shelf decelerated with clear seasonal  
578 variability associated with the presence of the fast ice (Fig 2). The loss of fast ice can affect the seasonal variability of velocity  
579 and calving dynamics of ice shelves, as seen for the Totten Ice Shelf (Greene et al., 2018) and Parker Ice Tongue (Gomez-Fell  
580 et al., 2022). Due to the fast ice moving as a cohesive unit coupled with the lack of iceberg rotation embedded in the fast ice,  
581 suggests a degree of mechanical coupling of the glacier tongues, and Scar Inlet Ice Shelf, to the fast ice, similar to the  
582 relationship of mélange and multiyear fast ice for the Voyeykov Ice Shelf prior to disaggregation (Arthur et al., 2021). The  
583 Larsen B fast ice played an integral role in the growth, deceleration, and stability of the Larsen B outlet glaciers, their floating  
584 tongues, and the Scar Inlet Ice Shelf. Given that the fast ice was 5-10 m thick, it likely provided backstress greater than the  $10^7$   
585  $\text{N m}^{-1}$  threshold required to suppress calving (Robel, 2017). Contrary to recent modelling results (Sun et al., 2023; Surawy-  
586 Stepney et al., 2023), in absence of any other plausible cause, our observations show the loss of the fast ice led directly to  
587 dramatic dynamical changes in the aforementioned tributary glaciers tongues and thereafter the subsequent grounded glaciers.

588  
589 According to de Rydt et al. (2015), an “immediate” glacier response is one that occurs  $< 2$  years after an initial event. Here we  
590 see an immediate disaggregation of the glacier tongues after the fast ice broke out. These responses mimic Voyeykov Ice Shelf  
591 where over the course of several months the ice shelf lost stabilizing land fast ice, then mélange, followed by partial loss of  
592 the ice shelf (Arthur et al., 2021). The immediate complete disaggregation of multiple floating ice tongues after the loss of the  
593 fast ice suggests that the fast ice was not only preventing calving but also supplied sufficient backstress that essentially held  
594 the tongues together. The glacier speeds began to gradually increase after the loss of their thick floating tongues (Fig. 9).

595  
596 The calving regimes and dynamical changes of the Larsen B tributary glaciers are similar to their response after the 2002  
597 Larsen B ice shelf disintegration, suggesting that calving is an immediate response to stress perturbations (Hulbe et al. 2008).  
598 At first glance, the two events were quite different; for example, the tributary glaciers were stable prior to the 2002 event and

599 though they were readvancing and stabilizing prior to the 2022 event they were still in an imbalanced state (Seehaus et al.,  
600 2023), additionally the ice shelf was old and thick whereas the fast ice was much younger and an order of magnitude thinner.  
601 However, despite these differences, the similarities in the tributary glacier response to the two events are important to identify.

602  
603 Crane Glacier experienced significant changes after the Larsen B Ice Shelf disintegration and fast ice break-out. In the three  
604 years following the Larsen B Ice Shelf disintegration event (2002 to 2005), the Crane Glacier ice front and grounding zone  
605 retreated 18 km into the fjord, and the ice front height increased from 60 m to just over 100 m (Scambos et al., 2011, De Rydt  
606 et al., 2015). Simultaneously, the glacier trunk upstream of the ice front lost elevation at a rate of 35 m yr<sup>-1</sup> (Shuman et al.,  
607 2011). As of March 2023, the 2022 event has caused Crane Glacier to retreat ~11 km in 14 months (Fig. 8). However,  
608 significant thinning in the upstream areas has yet to occur (Fig. 10). Between 2002 and 2003, Crane Glacier ice flow increased  
609 rapidly, roughly 3-fold from ~500 m yr<sup>-1</sup> to ~1500 m yr<sup>-1</sup> (Rignot et al., 2004). In 2007, Crane's terminus had speeds up to ~  
610 3500 m yr<sup>-1</sup> with a steady deceleration the following years (Wuite et al., 2015). By 2017 terminus speeds were ~1000 m yr<sup>-1</sup>  
611 (Rott et al., 2020) and remained that way until the break-out. In what is likely grounded ice (relative to both the grounding  
612 zone locations in this study and in Rott et al., 2018), speeds prior to the break-out were ~750 m yr<sup>-1</sup> and subsequently increased  
613 to ~1050 m yr<sup>-1</sup> by early 2023 (Fig. 9). Crane Glacier has responded similarly to the two episodes of buttressing loss in the last  
614 20 years, although the magnitude of change was greater in the immediate aftermath of the 2002 event (Fig. 12).

615  
616 Hektoria's calving in 2022 is similar to the 2002 event where initially floating tabular bergs calved and then an arcuate calving  
617 front formed with large rifts and slumping. In 2022/2023, Hektoria retreated ~25 km, with ~10 km of that retreat (or 1 to 5 km  
618 referencing the Rott et al.'s 2016 grounding line (Rott et al., 2018); Fig. 8) likely to be partially grounded ice on an ice plain  
619 (Tuckett et al., 2020). This is greater than the 2002 event in which Hektoria lost ~15 km of floating ice in the first year and it  
620 was not until a year after the loss of the ice shelf in 2003 that Hektoria began calving at its grounded terminus (Rack and Rott,  
621 2004). This could possibly be explained with the lower Hektoria glacier being much closer to floatation in 2022 than it was in  
622 2002 and possibly with a higher amount of accumulated damage. In that case, acceleration and thinning would have first been  
623 needed to bring the Hektoria Glacier to a height near floatation before significant retreat of grounded ice could occur after the  
624 2022 event. In 2002 to 2003 Hektoria's ice flow speeds increased 8-fold from ~250 m yr<sup>-1</sup> to over ~2000 m yr<sup>-1</sup>. Hektoria's  
625 terminus retreat paused from 2007 to 2009 and then reactivated in 2009 until the long-term fast ice formed in the embayment  
626 and stabilized the front in 2011 (Fig. 12). Following the fast ice breakout several kilometers upstream of the grounding line,  
627 Hektoria's ice flow speeds increased from 400 m yr<sup>-1</sup> to ~900 m yr<sup>-1</sup> (Fig. 9). Although the magnitude is not as great as the  
628 2002 event, the glaciers have had a dramatic acceleration. Hektoria's thinning from 2002 to 2003 was between 5 to 38 m yr<sup>-1</sup>  
629 (Scambos et al., 2004), whereas the 2022 event resulted in thinning of between 8 to 11 m on Green Glacier from March 2022  
630 to January 2023 (Fig. 11). Again, this is a similar and only slightly subdued response to the loss of embayment ice.

631

632 Both Crane and Hektoria experienced rapid changes after both the 2002 and 2022 events. The speed up of both glaciers was  
633 immediate, yet gradual, as the evolution of the system adjusted to new geometry, particularly the glacier bed. This gradual,  
634 slightly delayed increase in velocity may be why Sun et al. (2023) did not capture the acceleration as their velocity data ended  
635 in July/August 2022 and the majority of the acceleration took place after that (Fig. 9). However, that is along the same timeline  
636 of changes experienced in the 2002 event as the first velocity data was only available December 2002, nine months after the  
637 ice shelf break-up (Wuite et al., 2015). Comparison of the speeds, thinning, and retreat rates, reveals that the 2002 event had a  
638 greater impact on the glacier dynamics within the first year of the loss of ice shelf/multi-year fast ice buttressing. This is an  
639 expected response, as the loss of the Larsen B Ice Shelf should result in a higher de-buttressing effect than the more recent loss  
640 of the much thinner fast ice and thick glacier tongues.

## 641 **6 Conclusions**

642 The climate of the AP has been warming over the past several decades (Vaughan et al., 2003; Zagorodnov et al., 2012),  
643 interrupted by a decade-scale cooling that coincided with the formation of the fast ice in 2011 (Turner et al., 2016). During the  
644 2021/2022 summer, the Larsen B region of the AP experienced anomalously high temperatures, and strong westerly winds  
645 contributed to an ice-free corridor to open along the eastern coast of the Peninsula that in turn allowed long-period high  
646 amplitude ocean swell to reach the fast ice. In the 2021/2022 summer the Antarctic sea ice extent was at its lowest sea ice  
647 extent in the satellite record (prior to 2023) with the Weddell Sea contributing 26% to that negative anomaly (Turner et al.,  
648 2022). The sea ice extent in the Weddell Sea in 2022 was the 12<sup>th</sup> lowest in the satellite record (Turner et al., 2022) and the  
649 pack ice area immediately near the Larsen B embayment was at its lowest since 2010.

651 The large-amplitude wave event with a long period swell that occurred 18 to 19 January reached the fast ice front via the pack  
652 ice-free corridor. We infer that this flexed the fast ice, causing it to fracture and redistribute the stresses within the thin ice  
653 plate, which would be seasonally at its weakest due to the recent warm air temperature. We note, however, that surface  
654 meltwater-induced flexure and hydrofracture of the glacier tongues do not appear to play a direct role in this case. An AR and  
655 foehn wind event occurred during and after the fast ice break-out, contributing to the quick removal of the fast ice from the  
656 embayment.

657  
658 All of the glacier responses following the Larsen B embayment fast ice break-out are reminiscent of the effects on glacier flow  
659 and decreased surface elevation after the Larsen B ice shelf removal (i.e., extreme and varied; Rignot et al., 2004; Scambos et  
660 al., 2004), despite the fast ice being substantially thinner than the ice shelf (5 to 10 m compared to ~250 m; Fig. 1) and the  
661 glaciers being in different states prior to the break-outs (Seehaus et al., 2023). We conclude that the fast ice slab was acting to  
662 significantly buttress the glaciers' floating tongues, and its removal led to the disaggregation of the tongues and destabilization  
663 and dynamical changes of the grounded glaciers.

664

665 Antarctica's coastline is fringed with multi-year fast ice (Fraser et al., 2021) that is likely buttressing large glaciers around the  
666 continent. As the climate continues to change (Gilbert and Kittel, 2021), Antarctica's fast ice may become more susceptible to  
667 breakup due to increasing exposure to ocean swells via open-ocean corridors through pack ice (Reid and Massom, 2022; Teder  
668 et al., 2022). As Antarctic overall sea ice concentrations are projected to decrease over the current century (Holmes et al.,  
669 2022), this risk is inherently higher. Antarctic-wide fast-ice-buttressed glaciers will likely be subject to substantial dynamical  
670 changes and potential retreat if pack ice decline leads to multi-year fast ice break up.

671

672 This case study affirms the importance of examining the impacts of large-scale circulation patterns on foehn conditions, overall  
673 sea ice area, and ocean swells on the AP and other vulnerable ice shelf and outlet glacier areas. It is important to continue  
674 monitoring not only the glaciers feeding into the Larsen B embayment in terms of their response to changing fast ice conditions,  
675 but also other key glacier-ice shelf-fast ice interactive systems around Antarctica and their response to increased coastal  
676 exposure (Reid and Massom, 2022; Teder et al., 2022)

#### 677 **Supplemental Information**

678 Supplemental information can be found in tc-2023-88-supplement-version2.pdf.

#### 679 **Acknowledgements**

680 We would like to thank Chris Shuman and Mark Fahnestock for their help in monitoring the break-out and suggesting  
681 processing tools, as well as Bertie Miles for the suggestion on how to extract velocity profiles. We also thank the British  
682 Antarctic Survey pilots who captured images of the initial fast ice break-up on 31 January 2022, and the NSIDC for data access  
683 and technical support. NEO and TAS received support from NASA award 80NSSC22K0386 and USGS award 140G0118.  
684 AFB received support from the U.S. National Science Foundation (NSF) under award no. 1841607. GPS data was collected  
685 using the LARISSA award NSF OPP 0732602 and NSF OPP 0732921.

#### 686 **Author Contributions:**

687 NEO led the study, processed and analyzed the data, and led the writing of the manuscript. TAS initiated the idea and outlined  
688 the direction of the study with early data. GP processed the raw AMSR data to detect liquid water and AFB analyzed these  
689 data and produced Figure 5. RSA, SM, and LM contributed to the plan of the research. MLM analyzed the AR events. JAS  
690 contributed to the climate analysis methods. MT and ECP processed and analyzed the GPS data. All authors contributed to the  
691 writing of the manuscript and discussion of results.

692 **Competing interests:**

693 The authors declare no conflict of interest.

694 **Data Availability**

695 Sea ice concentration and extent data are available on the University of Bremen sea ice webpage ([https://seaice.uni-](https://seaice.uni-bremen.de/sea-ice-concentration/amsre-amsr2)  
696 [bremen.de/sea-ice-concentration/amsre-amsr2](https://seaice.uni-bremen.de/sea-ice-concentration/amsre-amsr2)). Operation IceBridge data is available at NSIDC  
697 (<https://nsidc.org/data/icebridge>) as well as the ICESat-2 data (<https://nsidc.org/data/at106/versions/6>). MODIS imagery can  
698 be viewed and downloaded on the Worldview interface (<https://worldview.earthdata.nasa.gov>). ERA-5 data are available at  
699 the Copernicus data store (<https://cds.climate.copernicus.eu/cdsapp#!/home>). WaveWatch III data are available on CSIRO  
700 (<https://data.csiro.au/collection/csiro:39819>). The AMSR-E/2 data are available to download here: [https://perscido.univ-](https://perscido.univ-grenoble-alpes.fr/datasets/DS391)  
701 [grenoble-alpes.fr/datasets/DS391](https://perscido.univ-grenoble-alpes.fr/datasets/DS391). The Reference Elevation Model of Antarctica is available via the Polar Geospatial Center  
702 (Howat et al., 2022, <https://www.pgc.umn.edu/data/rema/>). The Worldview DEMs are available from Polar Geospatial Center  
703 upon request.

704 **References**

705 Adusumilli, S., Fricker, H. A., Siegfried, M. R., Padman, L., Paolo, F. S., and Ligtenberg, S. R. M.: Variable basal melt rates  
706 of Antarctic Peninsula ice shelves, 1994–2016. *Geophys. Res. Lett.*, 45, 4086–4095. doi:[10.1002/2017GL076652](https://doi.org/10.1002/2017GL076652), 2018.

707  
708 Amundson, J. M., Fahnestock, M., Truffer, M., Brown, J., Lüthi, M. P., and Motyka, R. J.: Ice mélange dynamics and  
709 implications for terminus stability, Jakobshavn Isbræ, Greenland, *J. Geophys. Res.*, 115, F01005, doi:[10.1029/2009JF001405](https://doi.org/10.1029/2009JF001405),  
710 2010.

711  
712 Arthur, J., Stokes, C., Jamieson, S., Miles, B., Carr, J., and Leeson, A.: The triggers of the disaggregation of Voyeykov Ice  
713 Shelf (2007), Wilkes Land, East Antarctica, and its subsequent evolution, *J. Glaciol.*, 67(265), 933-951.  
714 doi:[10.1017/jog.2021.45](https://doi.org/10.1017/jog.2021.45), 2021.

715  
716 Banwell, A. F., MacAyeal, D. R., and Sergienko, O. V.: Breakup of the Larsen B Ice Shelf triggered by chain reaction drainage  
717 of supraglacial lakes, *Geophys. Res. Lett.*, 40, 5872– 5876, doi:[10.1002/2013GL057694](https://doi.org/10.1002/2013GL057694), 2013.

718  
719 Banwell, A. F. and Macayéal, D. R.: Ice-shelf fracture due to viscoelastic flexure stress induced by fill/drain cycles of  
720 supraglacial lakes, *Antarct. Sci.*, 27(6), 587-597, doi:[10.1017/S0954102015000292](https://doi.org/10.1017/S0954102015000292), 2015.

721

722 Banwell, A. F., Willis, I. C., Goodsell, B., Macdonald, G. J., Mayer, D., Powell, A. and MacAyeal, D. R.: Calving and Rifting  
723 on McMurdo Ice Shelf, Antarctica, *Ann. Glaciol.*, 58(75pt1), 78-87, doi:10.1017/aog.2017.12, 2017.

724

725 Banwell, A. F., Datta, R. T., Dell, R. L., Moussavi, M., Brucker, L., Picard, G., Shuman, C. A., and Stevens, L. A.: The 32-  
726 year record-high surface melt in 2019/2020 on the northern George VI Ice Shelf, Antarctic Peninsula, *Cryosphere*, 15, 909–  
727 925, doi:10.5194/tc-15-909-2021, 2021.

728

729 Banwell, A.F., Wever, N., Dunmire, D., and Picard, G.: Quantifying Antarctic-wide ice-shelf surface melt volume using  
730 microwave and firn model data: 1980 to 2021, *Geophys. Res. Lett.*, doi:10.1029/2023GL102744, 2023.

731

732 Bassis, J. N., Berg, B., Crawford, A. J., and Benn, D. I.: Transition to marine ice cliff instability controlled by ice thickness  
733 gradients and velocity, *Science*, 372(6548), 1342– 1344. doi:10.1126/science.abf6271, 2021.

734

735 Benn, D. I., Åström, J., Zwinger, T., Todd, J., Nick, F. M., Cook, S., Hulton, N. R. and Luckman, A.: Melt-under-cutting and  
736 buoyancy-driven calving from tidewater glaciers: New insights from discrete element and continuum model simulations, *J.*  
737 *Glaciol.*, 63(240), 691-702. doi:10.1017/jog.2017.41, 2017.

738

739 Berthier, E., Scambos, T. A., and Shuman, C. A.: Mass loss of Larsen B tributary glaciers (Antarctic Peninsula) unabated since  
740 2002, *Geophys. Res. Lett.*, 39(13), 1–6. doi:10.1029/2012GL051755, 2012.

741

742 Bevan, S. L., Luckman, A. J., Kuipers Munneke, P., Hubbard, B., Kulesa, B., and Ashmore, D. W.: Decline in surface melt  
743 duration on Larsen C Ice Shelf revealed by the advanced scatterometer (ASCAT), *Earth Space Sci.*, 5, 578–591.  
744 doi:10.1029/2018EA000421, 2018.

745

746 Borstad, C. P., Rignot, E., Mouginot, J. and Schodlok, M. P.: Creep deformation and buttressing capacity of damaged ice  
747 shelves: theory and application to Larsen C ice shelf, *Cryosphere*, 7(6), 1931-1947, doi:10.5194/tc-7-1931-2013, 2013.

748

749 Bozkurt, D., Rondanelli, R., Marin, J. C., and Garreaud, R.L: Foehn event triggered by an atmospheric river underlies record-  
750 setting temperature along continental Antarctica, *J. Geophys. Res. Atmos*, 123, 3871–3892. doi:10.1002/2017JD027796,  
751 2018.

752

753 Braun, M., Humbert, A., and Moll, A.: Changes of Wilkins Ice Shelf over the past 15 years and inferences on its stability, *The*  
754 *Cryosphere*, 3, 41–56, https://doi.org/10.5194/tc-3-41-2009, 2009

755

756 Cape, M. R., Vernet, M., Skvarca, P., Marinsek, S., Scambos, T. and Domack, E.: Foehn winds link climate-driven warming  
757 to ice shelf evolution in Antarctica, *J. Geophys. Res. Atmos.*, 120(21), 11-037, doi:[10.1002/2015JD023465](https://doi.org/10.1002/2015JD023465), 2015.

758

759 Carrasco, J. F., Bozkurt, D., and Cordero, R.: A review of the observed air temperature in the Antarctic Peninsula. Did the  
760 warming trend come back after the early 21st hiatus?, *Polar Sci.*, 28, 100653. doi: 0.1016/j.polar.2021.100653, 2021.

761

762 Cassotto, R., Fahnestock, M., Amundson, J., Truffer, M., and Joughin, I.: Seasonal and interannual variations in ice mélange  
763 and its impact on terminus stability, Jakobshavn Isbræ, Greenland, *J. Glaciol.*, 61(225), 76-88. doi:10.3189/2015JoG13J235,  
764 2015.

765

766 Cook, A. J. and Vaughan, D. G.: Overview of areal changes of the ice shelves on the Antarctic Peninsula over the past 50  
767 years, *Cryosphere*, 4(1), 77-98, doi:[10.5194/tc-4-77-2010](https://doi.org/10.5194/tc-4-77-2010), 2010.

768

769 Crawford, A. J., Benn, D. I., Todd, J., Åström, J. A., Bassis, J. N., and Zwinger, T.: Marine ice-cliff instability modelling  
770 shows mixed-mode ice-cliff failure and yields calving rate parameterization, *Nat. Comm.*, 12(1), 2701,  
771 <https://doi.org/10.1038/s41467-021-23070-7>, 2021

772

773 Datta, R. T., Tedesco, M., Fettweis, X., Agosta, C., Lhermitte, S., Lenaerts, J. T. M., and Wever, N.: The effect of Foehn-  
774 induced surface melt on firm evolution over the northeast Antarctic peninsula, *Geophys. Res. Lett.*, 46, 3822– 3831,  
775 doi:[10.1029/2018GL080845](https://doi.org/10.1029/2018GL080845), 2019.

776

777 Doake, C., and Vaughan, D.: Rapid disintegration of the Wordie Ice Shelf in response to atmospheric warming, *Nature*, 350,  
778 328–330, doi:10.1038/350328a0, 1991.

779

780 Fahnestock, M., Scambos, T., Moon, T., Gardner, A., Haran, T., and Klinger, M.: Rapid large-area mapping of ice flow using  
781 Landsat 8, *Remote Sens Environ.*, 185, 84-94. doi:10.1016/j.rse.2015.11.023, 2016.

782

783 Fogt, R. L., and Marshall, G. J.: The Southern Annular Mode: Variability, trends, and climate impacts across the Southern  
784 Hemisphere. *Rev. Clim. Change*, 11(4), 1–24. doi:[10.1002/wcc.652](https://doi.org/10.1002/wcc.652), 2020.

785

786 Fox, C., and Squire, V. A.: Coupling between the ocean and an ice shelf. *Ann. Glaciol.*, 15, 101-108, doi:10.3189/1991AoG15-  
787 1-101-108, 1991.

788



789 Friedl, P., Weiser, F., Fluhner, A., and Braun, M. H.: Remote sensing of glacier and ice sheet grounding lines: A review, *Earth-*  
790 *Sci. Rev.*, 201, 102948, <https://doi.org/10.1016/j.earscirev.2019.102948>, 2020.

791

792 Francis, D., Mattingly, K. S., Lhermitte, S., Temimi, M., and Heil, P.: Atmospheric extremes caused high oceanward sea  
793 surface slope triggering the biggest calving event in more than 50 years at the Amery Ice Shelf, *The Cryosphere*, 15, 2147–  
794 2165, <https://doi.org/10.5194/tc-15-2147-2021>, 2021

795

796 Francis, D., Fonseca, R., Mattingly, K. S., Marsh, O. J., Lhermitte, S., and Cherif, C.: Atmospheric triggers of the Brunt Ice  
797 Shelf calving in February 2021, *J. Geophys. Res. Atmos*, 127, e2021JD036424. <https://doi.org/10.1029/2021JD036424>, 2022.

798

799 Fraser, A. D., Massom, R. A., Handcock, M. S., Reid, P., Ohshima, K. I., Raphael, M. N., Cartwright, J., Klekociuk, A. R.,  
800 Wang, Z., and Porter-Smith, R.: Eighteen-year record of circum-Antarctic landfast-sea-ice distribution allows detailed baseline  
801 characterisation and reveals trends and variability, *Cryosphere*, 15, 5061–5077, doi:10.5194/tc-15-5061-2021, 2021.

802

803 Gardner, A. S., Moholdt, G., Scambos, T., Fahnestock, M., Ligtenberg, S., Broeke, M.V.D. and Nilsson, J.: Increased West  
804 Antarctic and unchanged East Antarctic ice discharge over the last 7 years. *Cryosphere*, 12(2), 521-547. doi:[10.5194/tc-12-](https://doi.org/10.5194/tc-12-521-2018)  
805 [521-2018](https://doi.org/10.5194/tc-12-521-2018), 2018.

806

807 Gilbert, E., and Kittel, C.: Surface melt and runoff on Antarctic ice shelves at 1.5°C, 2°C, and 4°C of future warming. *Geophys.*  
808 *Res. Lett.*, 48, e2020GL091733, <https://doi.org/10.1029/2020GL091733>, 2021.

809

810 Glasser, N. F. and Scambos, T. A.: A structural glaciological analysis of the 2002 Larsen B ice-shelf collapse, *J. Glaciol.*,  
811 54(184), 3-16, doi:10.3189/002214308784409017, 2008.

812

813 Glasser, N. F., Scambos, T. A., Bohlander, J., Truffer, M., Pettit, E., and Davies, B. J.: From ice-shelf tributary to tidewater  
814 glacier: continued rapid recession, acceleration and thinning of Röhss Glacier following the 1995 collapse of the Prince Gustav  
815 Ice Shelf, Antarctic Peninsula. *J. Glaciol.*, 57(203), 397–406, doi:10.3189/002214311796905578, 2011.

816

817 Gomez-Fell, R., Rack, W., Purdie, H., and Marsh, O.: Parker Ice Tongue collapse, Antarctica, triggered by loss of stabilizing  
818 land-fast sea ice. *Geophys. Res. Lett.*, 49, e2021GL096156. [doi:10.1029/2021GL096156](https://doi.org/10.1029/2021GL096156), 2022.

819

820 Hersbach, H., Bell, B., Berrisford, P., et al.: The ERA5 global reanalysis. *Q J R Meteorol Soc.*, 146. 1999–2049.  
821 <https://doi.org/10.1002/qj.3803>, 2020.

822

823 Holmes, C. R., Bracegirdle, T. J., and Holland, P. R.: Antarctic sea ice projections constrained by historical ice cover and  
824 future global temperature change. *Geophys. Res. Lett.*, 49, e2021GL097413. doi:[10.1029/2021GL097413](https://doi.org/10.1029/2021GL097413), 2022.

825

826 Howat, I., Porter C., Noh, M.-J., Erik, H., Samuel, K., Danish, E., Tomko, K., Gardiner, J., Negrete, A., Yadav, B., Klassen,  
827 J., Kelleher, C., Cloutier, M., Bakker, J., Enos, J., Arnold, G., Bauer, G., Morin, P.: The Reference Elevation Model of  
828 Antarctica - Strips, Version 4.1, Harvard Dataverse, V1, doi:[10.7910/DVN/X7NDNY](https://doi.org/10.7910/DVN/X7NDNY), 2022.

829

830 Hulbe, C. L., Scambos, T. A., Youngberg, T. and Lamb, A.K.: Patterns of glacier response to disintegration of the Larsen B  
831 ice shelf, Antarctic Peninsula. *Glob Planet Change*, 63(1), 1-8, doi:[10.1016/j.gloplacha.2008.04.001](https://doi.org/10.1016/j.gloplacha.2008.04.001), 2008.

832

833 Jeffries, M. O.: Arctic ice shelves and ice islands: origin, growth and disintegration, physical characteristics, structural-  
834 stratigraphic variability, and dynamics. *Rev. Geophys.* 30(3), 245–267. doi:[10.1029/92RG00956](https://doi.org/10.1029/92RG00956), 1992.

835

836 Khazendar, A., Rignot, E. and Larour, E.: Larsen B Ice Shelf rheology preceding its disintegration inferred by a control method.  
837 *Geophys. Res. Lett.*, 34(19), doi:[10.1029/2007GL030980](https://doi.org/10.1029/2007GL030980), 2007.

838

839 King, J. C., Turner, J., Marshall, G. J., Connolley, W. M. and Lachlan-Cope, T. A.: Antarctic Peninsula climate variability and  
840 its causes as revealed by analysis of instrumental records. *Antarct. Res. Ser.*, 79, 17-30, doi:[10.1029/AR079p0017](https://doi.org/10.1029/AR079p0017), 2003.

841

842 Kwon, H., Choi, H., Kim, B.M., Kim, S.W. and Kim, S.J.: Recent weakening of the southern stratospheric polar vortex and  
843 its impact on the surface climate over Antarctica. *Environ. Res. Lett.*, 15(9), 094072, doi:10.1088/1748-9326/ab9d3d, 2020.

844 Laffin, M. K., Zender, C. S., van Wessem, M., and Marinsek, S.: The role of föhn winds in eastern Antarctic Peninsula rapid  
845 ice shelf collapse, *Cryosphere*, 16, 1369–1381, doi:10.5194/tc-16-1369-2022, 2022.

846

847 Langhorne, P.J., Squire, V.A., Fox, C. and Haskell, T.G., 2001. Lifetime estimation for a land-fast ice sheet subjected to ocean  
848 swell. *Annals of Glaciology*, 33, 333, <https://doi.org/10.3189/172756401781818419>.

849

850 Larour, E., Rignot, E., Poinelli, M., and Scheuchl, B.: Physical processes controlling the rifting of Larsen C Ice Shelf,  
851 Antarctica, prior to the calving of iceberg A68. *PNAS*, 118 (40), e2105080118, <https://doi.org/10.1073/pnas.2105080118>,  
852 2021

853

854 Leeson, A. A., Van Wessem, J. M., Ligtenberg, S. R. M., Shepherd, A., Van Den Broeke, M. R., Killick, R., ... and Colwell,  
855 S.: Regional climate of the Larsen B embayment 1980-2014. *J. Glaciol.*, 63(240), 683–690.  
856 <https://doi.org/10.1017/jog.2017.39>, 2017.

857

858 Lei, Y., Gardner, A. and Agram, P.: Autonomous Repeat Image Feature Tracking (autoRIFT) and Its Application for Tracking  
859 Ice Displacement. *Remote Sens*, 13(4), 749. doi:[10.3390/rs13040749](https://doi.org/10.3390/rs13040749), 2021.

860

861 Li, X., Cai, W., Meehl, G. A., Chen, D., Yuan, X., Raphael, M., ... and Song, C.: Tropical teleconnection impacts on Antarctic  
862 climate changes, *Nat Rev Earth Environ*, 2(10), 680–698. doi:[10.1038/s43017-021-00204-5](https://doi.org/10.1038/s43017-021-00204-5), 2021.

863

864 Liang, K., Wang, J., Luo, H., and Yang, Q.: The role of atmospheric rivers in Antarctic sea ice variations. *Geophys. Res. Lett.*,  
865 50, e2022GL102588. <https://doi.org/10.1029/2022GL102588>, 2023.

866

867 van Lipzig, N. P. M., Marshall, G. J., Orr, A., and King, J. C.: The Relationship between the Southern Hemisphere Annular  
868 Mode and Antarctic Peninsula Summer Temperatures: Analysis of a High-Resolution Model Climatology. *J. Climate*, 21,  
869 1649–1668, doi:[10.1175/2007JCLI1695.1](https://doi.org/10.1175/2007JCLI1695.1), 2008

870

871 Marshall, G. J., Orr, A., van Lipzig, N. P., and King, J. C.: The Impact of a Changing Southern Hemisphere Annular Mode on  
872 Antarctic Peninsula Summer Temperatures. *J. Climate*, 19, 5388–5404, doi:[10.1175/JCLI3844.1](https://doi.org/10.1175/JCLI3844.1), 2006.

873

874 Massom, R. A., Giles, A. B., Fricker, H. A., Warner, R. C., Legrésy, B., Hyland, G., Young, N., and Fraser, A. D : Examining  
875 the interaction between multi-year fast ice and the Mertz Glacier Tongue, East Antarctica: Another factor in ice sheet stability?,  
876 *J. Geophys. Res.*, 115, C12027, doi:10.1029/2009JC006083, 2010.

877

878 Massom, R. A., Scambos, T. A., Bennetts, L. G., Reid, P., Squire, V. A., and Stammerjohn, S. E.: Antarctic ice shelf  
879 disintegration triggered by sea ice loss and ocean swell, *Nature*, 558.7710, 383-389, doi:10.1038/s41586-018-0212-1 2018.

880

881 Meehl, G. A., Arblaster, J. M., Bitz, C. M., Chung, C. T. & Teng, H.: Antarctic sea- ice expansion between 2000 and 2014  
882 driven by tropical Pacific decadal climate variability. *Nat. Geosci.* 9, 590–595, doi:10.1038/ngeo2751, 2016.

883

884 Meier, W. N., T. Markus, and J. C. Comiso.: AMSR-E/AMSR2 Unified L3 Daily 12.5 km Brightness Temperatures, Sea Ice  
885 Concentration, Motion & Snow Depth Polar Grids, Version 1. Boulder, Colorado USA. NASA National Snow and Ice Data  
886 Center Distributed, Active Archive Center. Accessed May 2022. doi:10.5067/RA1MIJOYPK3P, 2018.

887

888 Melton, S., Alley, R., Anandakrishnan, S., Parizek, B., Shahin, M., Stearns, L., . . . Finnegan, D.: Meltwater drainage and  
889 iceberg calving observed in high-spatiotemporal resolution at Helheim Glacier, Greenland. *J. Glaciol.*, 68(270), 812-828,  
890 doi:10.1017/jog.2021.141, 2022.

891

892 Mercer, J. H.: West Antarctic ice sheet and CO<sub>2</sub> greenhouse effect: a threat of disaster, *Nature*, 271, 321–325,  
893 <https://doi.org/10.1038/271321a0>, 1978.

894

895 Miles, B. W. J., Stokes, C. R., and Jamieson, S. S. R.: Simultaneous disintegration of outlet glaciers in Porpoise Bay (Wilkes  
896 Land), East Antarctica, driven by sea ice break-up, *The Cryosphere*, 11, 427–442, <https://doi.org/10.5194/tc-11-427-2017>,  
897 2017.

898

899 Miles, B. W. J., Stokes, C. R., and Jamieson, S. S. R.: Velocity increases at Cook Glacier, East Antarctica, linked to ice shelf  
900 loss and a subglacial flood event, *The Cryosphere*, 12, 3123–3136, <https://doi.org/10.5194/tc-12-3123-2018>, 2018

901

902 Moon, T., Joughin, I., and Smith, B.: Seasonal to multiyear variability of glacier surface velocity, terminus position, and sea  
903 ice/ice mélange in northwest Greenland, *J. Geophys. Res. Earth Surf.*, 120, 818– 833. doi: [10.1002/2015JF003494](https://doi.org/10.1002/2015JF003494), 2015.

904

905 Murray, T., Selmes, N., James, T. D., Edwards, S., Martin, I., O'Farrell, T., Aspey, R., Rutt, I., Nettles, M., and Baugé, T.:  
906 Dynamics of glacier calving at the ungrounded margin of Helheim Glacier, southeast Greenland. *J. Geophys. Res. Earth Surf.*,  
907 120, 964–982. doi:[10.1002/2015JF003531](https://doi.org/10.1002/2015JF003531), 2015

908

909 Murty, T. S.: Modification of hydrographic characteristics, tides, and normal modes by ice cover. *Mar. Geod.*, 9(4), 451-468.  
910 doi:[10.1080/15210608509379538](https://doi.org/10.1080/15210608509379538), 1985.

911

912 Needell, C., and Holschuh, N.: Evaluating the retreat, arrest, and regrowth of Crane Glacier against marine ice cliff process  
913 models. *Geophys. Res. Lett.*, 50, e2022GL102400. <https://doi.org/10.1029/2022GL102400>, 2023.

914

915 Ochwat, N., Scambos, T., Fahnestock, M. and Stammerjohn, S.: Characteristics, recent evolution, and ongoing retreat of Hunt  
916 Fjord Ice Shelf, northern Greenland. *J. Glaciol.*, 69(273), 57-70, doi:10.1017/jog.2022.44, 2023a.

917

918 Ochwat, N., Banwell, A., and Scambos, T., Larsen B fast-ice breakout and initial glacier response [in “State of the Climate  
919 2023”]. *Antarctica and the Southern Ocean*, *Bull. Amer. Meteor. Soc.*, 104 (9), S349-S351, <https://doi.org/10.1175/BAMS-D-23-0077.1>, 2023b.

920

921

922 Orr, A., Marshall, G. J., Hunt, J. C. R., Sommeria, J., Wang, C., van Lipzig, N. P. M., Cresswell, D., and King, J. C.:  
923 Characteristics of Summer Airflow over the Antarctic Peninsula in Response to Recent Strengthening of Westerly Circumpolar  
924 Winds. *J. Atmos. Sci.*, 65, 1396–1413, <https://doi.org/10.1175/2007JAS2498.1>, 2008.

925

926 Parizek, B. R., Christianson, K., Alley, R. B., Voytenko, D., Vaňková, I., Dixon, T. H., ... and Holland, D. M.: Ice-cliff failure  
927 via retrogressive slumping, *Geology*, 47(5):449-452, doi:[10.1130/G45880.1](https://doi.org/10.1130/G45880.1), 2019.

928

929 Picard, G., Fily, M., and Gallee, H., 2007. Surface melting derived from microwave radiometers: A climatic indicator in  
930 Antarctica. *Ann. Glaciol.*, 46, 29-34. doi:10.3189/172756407782871684

931

932 Picard, G., Leduc-Leballeur, M., Banwell, A. F., Brucker, L., and Macelloni, G.: The sensitivity of satellite microwave  
933 observations to liquid water in the Antarctic snowpack, *Cryosphere*, 16, 5061–5083, doi:10.5194/tc-16-5061-2022, 2022.

934

935 Reeh, N., Thomsen, H., Higgins, A., and Weidick, A.: Sea ice and the stability of north and northeast Greenland floating  
936 glaciers. *Ann. Glaciol.*, 33, 474-480. doi:10.3189/172756401781818554, 2001.

937

938 Reid, P.A., and R.A. Massom.: Change and variability in Antarctic coastal exposure, 1979– 2020. *Nat Comm*, 13, 1164,  
939 <https://doi.org/10.1038/s41467-022-28676-z>, 2022.

940

941 Rignot, E., Casassa, G., Gogineni, P., Krabill, W., Rivera, A., and Thomas, R.: Accelerated ice discharge from the Antarctic  
942 Peninsula following the collapse of Larsen B ice shelf, *Geophys. Res. Lett.*, 31, L18401, doi:[10.1029/2004GL020697](https://doi.org/10.1029/2004GL020697), 2004.

943

944 Robel, A.A.: Thinning sea ice weakens buttressing force of iceberg mélange and promotes calving. *Nat. Comms.*, 8(1), 14596,  
945 doi:10.1038/ncomms14596, 2017.

946

947 Robinson, W. H. and Haskell, T. G.: Travelling flexural waves in the Erebus Glacier Tongue, McMurdo Sound, Antarctica,  
948 *Cold Reg Sci Technol*, 20.3, 289-293, doi:[10.1016/0165-232X\(92\)90035-S](https://doi.org/10.1016/0165-232X(92)90035-S), 1992.

949

950 Rott, H., Skvarca, P. and Nagler, T.: Rapid collapse of northern Larsen ice shelf, *Antarct. Sci.*, 271(5250), 788-792,  
951 doi:[10.1126/science.271.5250.788](https://doi.org/10.1126/science.271.5250.788), 1996.

952

953 Rott, H., Rack, W., Nagler, T. and Skvarca, P.: Climatically induced retreat and collapse of northern Larsen Ice Shelf, Antarctic  
954 Peninsula, *Ann. Glaciol.*, 27, 86-92, doi:[10.3189/S0260305500017262](https://doi.org/10.3189/S0260305500017262), 1998.

955

956 Rott, H., Abdel Jaber, W., Wuite, J., Scheiblauer, S., Floricioiu, D., Van Wessem, J. M., Nagler, T., Miranda, N., and Van Den  
957 Broeke, M. R.: Changing pattern of ice flow and mass balance for glaciers discharging into the Larsen A and B embayments,  
958 Antarctic Peninsula, 2011 to 2016, *Cryosphere*, 12(4), 1273–1291. doi:[10.5194/tc-12-1273-2018](https://doi.org/10.5194/tc-12-1273-2018), 2018.

959

960 Rott, H., Waite, J., De Rydt, J., Gudmundsson, G.H., Floricioiu, D., and Rack, W.; Impact of marine processes on flow  
961 dynamics of northern Antarctic Peninsula outlet glaciers, *Nat Comms.*, 11:2969,| doi:10.1038/s41467-020-16658-y, 2020.

962

963 De Rydt J., Gudmundsson G. H., Rott H., and Bamber J. L.: Modeling the instantaneous response of glaciers after the collapse  
964 of the Larsen B Ice Shelf, *Geophys. Res. Lett.*, 42(13):5355-5363, doi: [10.1002/2015GL064355](https://doi.org/10.1002/2015GL064355), 2015.

965

966 Scambos, T., Hulbe, C., and Fahnestock, M.: Climate-induced ice shelf disintegration in the Antarctic Peninsula, in: *Antarctic*  
967 *Peninsula Climate Variability: Historical and Paleoenvironmental Perspectives*. Antarctic Research Series, 79, edited by:  
968 Domack, E., Leventer, A., Burnett, A., Bindschadler, R., Convey, P., and Kirby, M., AGU, Washington, DC, 79–92,  
969 doi:[10.1029/AR079p0079](https://doi.org/10.1029/AR079p0079), 2003.

970

971 Scambos, T. A., Bohlander, J. A., Shuman, C. A., and Skvarca, P.: Glacier acceleration and thinning after ice shelf collapse in  
972 the Larsen B embayment, *Antarctica*, *Geophys. Res. Lett.*, 31, L18402, doi:[10.1029/2004GL020670](https://doi.org/10.1029/2004GL020670), 2004.

973

974 Scambos, T., R. Ross, R. Bauer, Y. Yermolin, P. Skvarca, D. Long, J. Bohlander, and T. Haran.: Calving and ice-shelf break-  
975 up processes investigated by proxy: Antarctic tabular iceberg evolution during northward drift, *J. Glaciol.*, 54(187), 579-591.  
976 doi:10.3189/002214308786570836, 2008.

977

978 Scambos, T., Fricker, H. A., Liu, C. C., Bohlander, J., Fastook, J., Sargent, A., Massom, R. and Wu, A. M.: Ice shelf  
979 disintegration by plate bending and hydro-fracture: Satellite observations and model results of the 2008 Wilkins ice shelf  
980 break-ups. *Earth Planet. Sci. Lett.*, 280(1-4), 51-60. doi:10.1016/j.epsl.2008.12.027, 2009.

981

982 Scambos, T.A., Ross, R., Haran, T., Bauer, R., Ainley, D.G., Seo, K.W., De Keyser, M., Behar, A. and MacAyeal, D.R.: A  
983 camera and multisensor automated station design for polar physical and biological systems monitoring: AMIGOS. *J. Glaciol.*,  
984 59(214). doi:10.3189/2013JoG12J170. 2013.

985

986 Scambos, T., Moussavi, M. S., Abdalati, W. and Pettit, E. C.: December. Evolution of fast ice thickness from Cryosat-2 radar  
987 altimetry data, a case study in Scar Inlet, Antarctica. AGU Fall Meeting Abstracts (Vol. 2017, pp. C21G-1181), 2017.

988

989 Seehaus, T. C., Sommer, C., Dethinne, T., and Malz, P.: Mass changes of the northern Antarctic Peninsula Ice Sheet derived  
990 from repeat bi-static SAR acquisitions for the period 2013–2017, *The Cryosphere Discuss.* [preprint], doi:10.5194/tc-2022-  
991 251, in review, 2023.

992

993 Shields, C. A., Wille, J. D., Marquardt Collow, A. B., MacLennan, M., and Gorodetskaya, I. V.: Evaluating uncertainty and  
994 modes of variability for Antarctic atmospheric rivers. *Geophys. Res. Lett.*, 49, e2022GL099577. doi:10.1029/2022GL099577,  
995 2022.

996

997 Shuman C. A., Berthier E., and Scambos T. A.: 2001-2009 Elevation and mass losses in the Larsen A and B embayments,  
998 Antarctic Peninsula, *J. Glaciol.*, 57(204):737-754. doi:10.3189/002214311797409811, 2011.

999

1000 Shuman, C., Scambos, T. and Berthier, E.: Ice loss processes in the Seal Nunataks ice shelf region from satellite altimetry and  
1001 imagery. *Ann. Glaciol*, 57(73), 94-104, doi:10.1017/aog.2016.29, 2016.

1002

1003 Skvarca, P., Rack, W., Rott, H. and Donángelo, T. I.: Climatic trend and the retreat and disintegration of ice shelves on the  
1004 Antarctic Peninsula: an overview, *Polar Res*, 18(2), 151-157, doi:10.1111/j.1751-8369.1999.tb00287, 1999.

1005

1006 [Smith, B., Fricker, H.A., Gardner, A.S., Medley, B., Nilsson, J., Paolo, F.S., Holschuh, N., Adusumilli, S., Brunt, K., Csatho,](#)  
1007 [B. and Harbeck, K.: Pervasive ice sheet mass loss reflects competing ocean and atmosphere processes. \*Science\*, 368\(6496\),](#)  
1008 [239-1242, doi:10.1126/science.aaz5845, 2020.](#)

1009

1010 Smith, B., S. Adusumilli, B. M. Csathó, D. Felikson, H. A. Fricker, A. Gardner, N. Holschuh, J. Lee, J. Nilsson, F. S. Paolo,  
1011 M. R. Siegfried, T. Sutterley, and the ICESat-2 Science Team: ATLAS/ICESat-2 L3A Land Ice Height, Version 5., Boulder,  
1012 Colorado USA. NASA National Snow and Ice Data Center Distributed Active Archive Center.  
1013 doi:10.5067/ATLAS/ATL06.005. Date Accessed 09-12-2022, 2021.

1014

1015 Spreen, G., Kaleschke, L., and Heygster, G.: Sea ice remote sensing using AMSR-E 89 GHz channels, *J. Geophys. Res.*, 113,  
1016 C02S03, doi:10.1029/2005JC003384, 2008.

1017

1018 Squire, V.A., 2007. Of ocean waves and sea-ice revisited. *Cold Regions Science and Technology*, 49(2), 110,  
1019 <https://doi.org/10.1016/j.coldregions.2007.04.007>.

1020

1021 Sun, Y., Riel, B., and Minchew, B.: Disintegration and buttressing effect of the landfast sea ice in the Larsen B embayment,  
1022 Antarctic Peninsula. *Geo. Res. Lett.*, 50, e2023GL104066. <https://doi.org/10.1029/2023GL104066>, 2023.

1023  
1024 Surawy-Stepney, T., Hogg, A. E., Cornford, S. L., Wallis, B. J., Davison, B. J., Selley, H. L., Slater, R. A. W., Lie, E. K.,  
1025 Jakob, L., Ridout, A. L., Gourmelen, N., Freer, B. I. D., Wilson, S. F., and Shepherd, A.: The impact of landfast sea ice  
1026 buttressing on ice dynamic speedup in the Larsen-B Embayment, Antarctica, *The Cryosphere Discuss.* [preprint],  
1027 <https://doi.org/10.5194/tc-2023-128>, in review, 2023.

1028  
1029 Teder, N. J., Bennetts, L. G., Reid, P. A., and Massom, R. A.: Sea ice-free corridors for large swell to reach Antarctic ice  
1030 shelves. *Environ. Res. Lett.*, 17(4), 045026, doi:10.1088/1748-9326/ac5edd, 2022.

1031  
1032 Torinesi, O., Fily, M., and Genthon, C.: Variability and Trends of the Summer Melt Period of Antarctic Ice Margins since  
1033 1980 from Microwave Sensors. *J. Climate*, 16, 1047–1060, doi:[10.1175/1520-0442\(2003\)016<1047:VATOTS>2.0.CO;2](https://doi.org/10.1175/1520-0442(2003)016<1047:VATOTS>2.0.CO;2),  
1034 2003.

1035  
1036 Turner, J., Lu, H., White, I., King, J. C., Phillips, T., Hosking, J. S., Bracegirdle, T. J., Marshall, G. J., Mulvaney, R. and Deb,  
1037 P.: Absence of 21st century warming on Antarctic Peninsula consistent with natural variability, *Nature*, 535, 411–415.  
1038 doi:[10.1038/nature18645](https://doi.org/10.1038/nature18645), 2016.

1039  
1040 Turner, J., Holmes, C., Caton Harrison, T., Phillips, T., Jena, B., Reeves-Francois, T., et al.: Record low Antarctic sea ice  
1041 cover in February 2022. *Geophys. Res. Lett.*, 49, e2022GL098904. doi:[10.1029/2022GL098904](https://doi.org/10.1029/2022GL098904), 2022.

1042  
1043 Van Wessem, J. M., Reijmer, C. H., Van De Berg, W. J., van Den Broeke, M. R., Cook, A. J., Van Uft, L. H. and Van  
1044 Meijgaard, E.: Temperature and wind climate of the Antarctic Peninsula as simulated by a high-resolution Regional  
1045 Atmospheric Climate Model. *J. Clim.*, 28(18), 7306–7326. doi:[10.1175/JCLI-D-15-0060.1](https://doi.org/10.1175/JCLI-D-15-0060.1), 2015.

1046  
1047 Wellner, J.S., Scambos, T., Domack, E.W., Vernet, M., Leventer, A., Balco, G., Brachfeld, S., Cape, M.R., Huber, B., Ishman,  
1048 S. and McCormick, M.L.: The Larsen ice shelf system, Antarctica (LARISSA): Polar systems bound together, changing fast.  
1049 *GSA Today*, 29(8). doi:10.1130/GSATG382A.1, 2019

1050  
1051 White, A., Copland, L., Mueller, D., and Van Wychen, W.: Assessment of historical changes (1959–2012) and the causes of  
1052 recent break-ups of the Petersen ice shelf, Nunavut, Canada. *Ann. Glaciol.*, 56(69), 65–76. doi:10.3189/2015AoG69A687,  
1053 2015.

1054  
1055 Wille, J. D., Favier, V., Dufour, A., Gorodetskaya, I. V., Turner, J., Agosta, C., and Codron, F.: West Antarctic surface melt  
1056 triggered by atmospheric rivers. *Nat. Geosci.* 12, 911–916, <https://doi.org/10.1038/s41561-019-0460-1>, 2019.



1057  
1058 Wille, J. D., Favier, V., Gorodetskaya, I. V., Agosta, C., Kittel, C., Beeman, J. C., Jourdain, N. C., Lenaerts, J. T. M., and  
1059 Codron, F.: Antarctic atmospheric river climatology and precipitation impacts. *J. Geophys. Atmos.*, 126, e2020JD033788.  
1060 doi:[10.1029/2020JD033788](https://doi.org/10.1029/2020JD033788), 2021.

1061  
1062 Wille, J. D., Favier, V., Jourdain, N. C., Kittel, C., Turton, J. V., Agosta, C., ... and Berchet, A.: Intense atmospheric rivers can  
1063 weaken ice shelf stability at the Antarctic Peninsula. *Nat. Commun Earth & Environ*, 3(1), doi:[10.1038/s43247-022-00422-9](https://doi.org/10.1038/s43247-022-00422-9),  
1064 2022.

1065  
1066 Wuite, J., Rott, H., Hetzenecker, M., Floricioiu, D., De Rydt, J., Gudmundsson, G. H., Nagler, T., and Kern, M.: Evolution of  
1067 surface velocities and ice discharge of Larsen B outlet glaciers from 1995 to 2013, *Cryosphere*, 9, 957–969, doi:10.5194/tc-9-  
1068 957-2015, 2015.

1069  
1070 Young, N., Turner, D., Hyland, G., and Williams, R.: Near-coastal iceberg distributions in East Antarctica, 50-145° E. *Ann.*  
1071 *Glaciol*, 27, 68-74. doi:10.3189/1998AoG27-1-68-74, 1998.

1072  
1073 Zagorodnov, V., Nagornov, O., Scambos, T.A., Muto, A., Mosley-Thompson, E., Pettit, E.C. and Tyufin, S.: Borehole  
1074 temperatures reveal details of 20th century warming at Bruce Plateau, Antarctic Peninsula. *Cryosphere*, 6(3), 675-686, doi:  
1075 10.5194/tc-6-675-2012, 2012.